MODELING, SIMULATION, AND ANALYSIS OF GRID CONNECTED DISH-STIRLING SOLAR POWER PLANTS

A Thesis
Presented to
The Academic Faculty

by

Dustin F. Howard

In Partial Fulfillment
of the Requirements for the Degree
Master of Science in the
School of Electrical and Computer Engineering

Georgia Institute of Technology
August 2010

MODELING, SIMULATION, AND ANALYSIS OF GRID CONNECTED DISH-STIRLING SOLAR POWER PLANTS

Approved by:

Dr. Ronald G. Harley, Advisor
School of Electrical and Computer Engineering
Georgia Institute of Technology

Dr. Thomas G. Habetler
School of Electrical and Computer Engineering
Georgia Institute of Technology

Dr. Deepakraj M. Divan
School of Electrical and Computer Engineering
Georgia Institute of Technology

Date Approved: July 6, 2010

To my mother, Kathy Howard, and my father, Fred Howard, for their enduring love, patience, and support.

ACKNOWLEDGEMENTS

Numerous individuals contributed with both technical and moral support for the completion of this thesis. The work presented here would not have been possible without their help.

Dr. Ronald G. Harley has been a constant source of technical guidance, and has spent many hours helping me better understand the fundamentals of power engineering. His patience and willingness to take time and delve into the technical details of this research cannot be appreciated enough. I would also like to thank Dr. Thomas Habetler and Dr. Deepak Divan for their guidance and inspiration as both professors and researchers.

I would like to thank the members of the Wesley Foundation at Georgia Tech and Rev. Steve Fazenbaker for providing a welcoming and encouraging place of faith. My success and overall positive experience of college life at Georgia Tech is largely attributed to the friendships and intellectual and spiritual growth that developed as a result of many hours spent at the Wesley Foundation.

I would like to thank my fellow lab mates for their technical assistance and ideas regarding this research, particularly Jiaqi Liang, who contributed much to the work included in this thesis, and helped improve on the modeling details. I would also like to thank by lab mates for our regular outings outside of lab, which helped support and sustain me through the somewhat difficult and stressful times that graduate student life can bring.

Most of all I would like to thank my sisters and my parents, who have been there for me through the best and worst of times throughout my life. During the time of this thesis work, I had the great sorrow of losing a grandfather and the joy of becoming an

uncle to twin boys. This work would not have been possible without the inspiration and encouragement that they have provided.

TABLE OF CONTENTS

LIST OF TABLES

Page

LIST OF FIGURES

Page

LIST OF SYMBOLS

Symbol	Meaning (units)
c	specific heat capacity (J/(kg*K))
d	derivative operator with respect to crank angle, diameter (m)
D	derivative operator with respect to time, pipe diameter (m)
f	friction factor
F	mechanical damping (kg*m^2/s)
gA	mass flow (kg/s)
h	heat transfer coefficient (W/(m^2*K))
I	irradiance (W/m^2)
J	moment of inertia (kg*m^2)
L	length (m)
m	mass (kg)
M	total mass of working gas inside Stirling engine (kg)
p	working gas pressure (Pa)
Q	heat (J)
R	gas constant (m^3*Pa/(K*kg))
T	temperature (K)
V	volume (m^3)
W	work (J)
α	displacement angle (rad)
ϕ	crank angle (rad)

η	efficiency
ρ	density (kg/m^3)
τ	torque (N*m)
ω	Shaft rotational speed (rad/s)

Subscript	**Meaning**
a	ambient
c	compression space
ck	compression space-cooler interface
con	concentrator
de, dc	dead space
elec	electric
e	expansion space
h	heater
he	heater-expansion space interface
I	input
k	cooler
kr	cooler-regenerator interface
L	losses
m	mirror
p	constant pressure, pipe
r	regenerator

rh	regenerator-heater interface
s	swept space
st	storage tank
v	constant volume

LIST OF ABBREVIATIONS

AVR	Automatic Voltage Regulator
CSP	Concentrating Solar Power
DIR	Direct Illuminated Receiver
DNI	Direct Normal Irradiance
DS	Dish-Stirling
EIA	Energy Information Adminstration
GIR	Grid Interconnection Requirements
IIR	Indirect Illuminated Receiver
LCOE	Levelized Cost Of Electricity
LVRT	Low-Voltage Ride Through
MM	Multi-Machine
NREL	National Renewable Energy Laboratory
OS	Over-Speed
PCC	Point of Common Coupling
PCS	Pressure Control System
PCU	Power Conversion Unit
PV	Photovoltaic
SAIC	Science Applications International Corp.
SBP	Schlaich Bergermann and Partner
SES	Stirling Energy Systems
SM	Single-Machine

SMIB	Single Machine Infinite Bus
STATCOM	Static Synchronous Compensator
SVC	Static Var Compensator
TCS	Temperature Control System

SUMMARY

The percentage of renewable energy within the global electric power generation portfolio is expected to increase rapidly over the next few decades due to increasing concerns about climate change, fossil fuel costs, and energy security. Solar thermal energy, also known as concentrating solar power (CSP), is emerging as an important solution to new demands for clean, renewable electricity generation. Dish-Stirling (DS) technology, a form of CSP, is a relatively new player in the renewable energy market, although research in the technology has been ongoing now for nearly thirty years. The first large plant utilizing DS technology, rated at 1.5 MW, came online in January 2010 in Peoria, AZ, and plants rated for several hundred MW are in the planning stages. Increasing capacity of this technology within the utility grid requires extensive dynamic simulation studies to ensure that the power system maintains its safety and reliability in spite of the technological challenges that DS technology presents, particularly related to the intermittency of the energy source and its use of a non-conventional asynchronous generator. The research presented in this thesis attempts to fill in the gaps between the well established research on Stirling engines in the world of thermodynamics and the use of DS systems in electric power system applications, a topic which has received scant attention in publications since the emergence of this technology.

DS technology uses a paraboloidal shaped dish of mirrors to concentrate sunlight to a single point. The high temperatures achieved at the focal point of the mirrors is used as a heat source for the Stirling engine, which is a closed-cycle, external heat engine.

Invented by the Scottish clergyman Robert Stirling in 1816, the Stirling engine is capable of high efficiency and releases no emissions, making it highly compatible with concentrated solar energy. The Stirling engine turns a squirrel-cage induction generator, where electricity is delivered through underground cables from thousands of independent, autonomous 10-25 kW rated DS units in a large solar farm.

A dynamic model of the DS system is presented in this thesis, including models of the Stirling engine working gas and mechanical dynamics. Custom FORTRAN code is written to model the Stirling engine dynamics within PSCAD/EMTDC. The Stirling engine and various other components of the DS system are incorporated into an electrical network, including first a single-machine, infinite bus network, and then a larger 12-bus network including conventional generators, loads, and transmission lines. An analysis of the DS control systems is presented, and simulation results are provided to demonstrate the system's steady state and dynamic behavior within these electric power networks. Potential grid interconnection requirements are discussed, including issues with power factor correction and low voltage ride-through, and simulation results are provided to illustrate the dish-Stirling system's capability for meeting such requirements.

CHAPTER 1

INTRODUCTION

1.1 Background

The amount of renewable energy integrated into the power grid is expected to increase significantly in upcoming years due to concerns about energy security and climate change. Solar energy will make up a substantial portion of this new renewable generation capacity, with anticipated growth in U.S. solar power generation capacity shown in Fig. 1.1 for both solar thermal and photovoltaic (PV) technologies through the year 2035 [1]. Solar thermal installations often have a larger generating capacity than PV installations since solar thermal is used exclusively in utility scale installations. PV, on the other hand, is used in residential, commercial, industrial, and utility applications, but typically has a generating capacity much smaller than solar thermal technologies. PV has

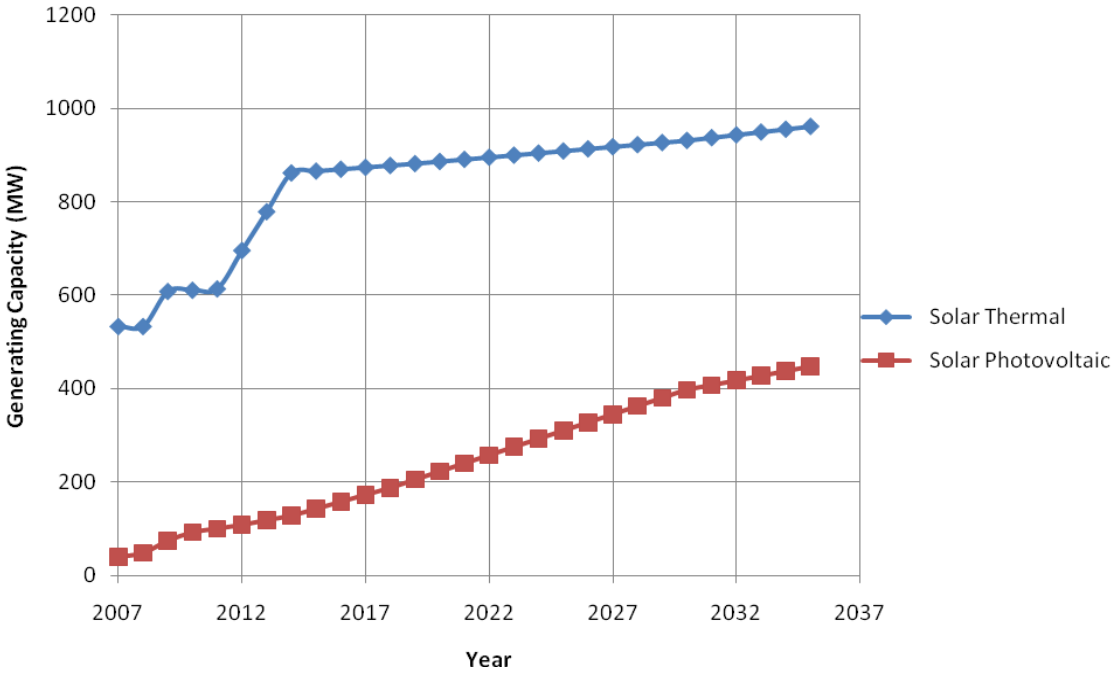

Figure 1.1: Estimated growth in generating capacity of solar thermal and photovoltaic technologies in the U.S. through the year 2035 [1].

a higher expected annual growth rate (8.6%) than solar thermal technologies (2.2%) through 2035, but the predicted levelized cost of electricity (LCOE) for solar thermal (256.6 $/MWh) is lower than PV (396.1 $/MWh) for plants entering service in 2016 [1]. The National Renewable Energy Laboratory (NREL) maintains a database of solar thermal projects in the U.S. [2], and gives a much higher capacity of solar thermal installations in the next five years than given in Fig. 1.1, indicating that the growth rates in [1] for solar power generation capacity may be quite conservative. Nevertheless, growth in solar power generating capacity is expected due to an increasing need for clean, renewable energy.

1.2 Solar Thermal Technologies

Solar thermal technologies, also known as concentrating solar power (CSP), use

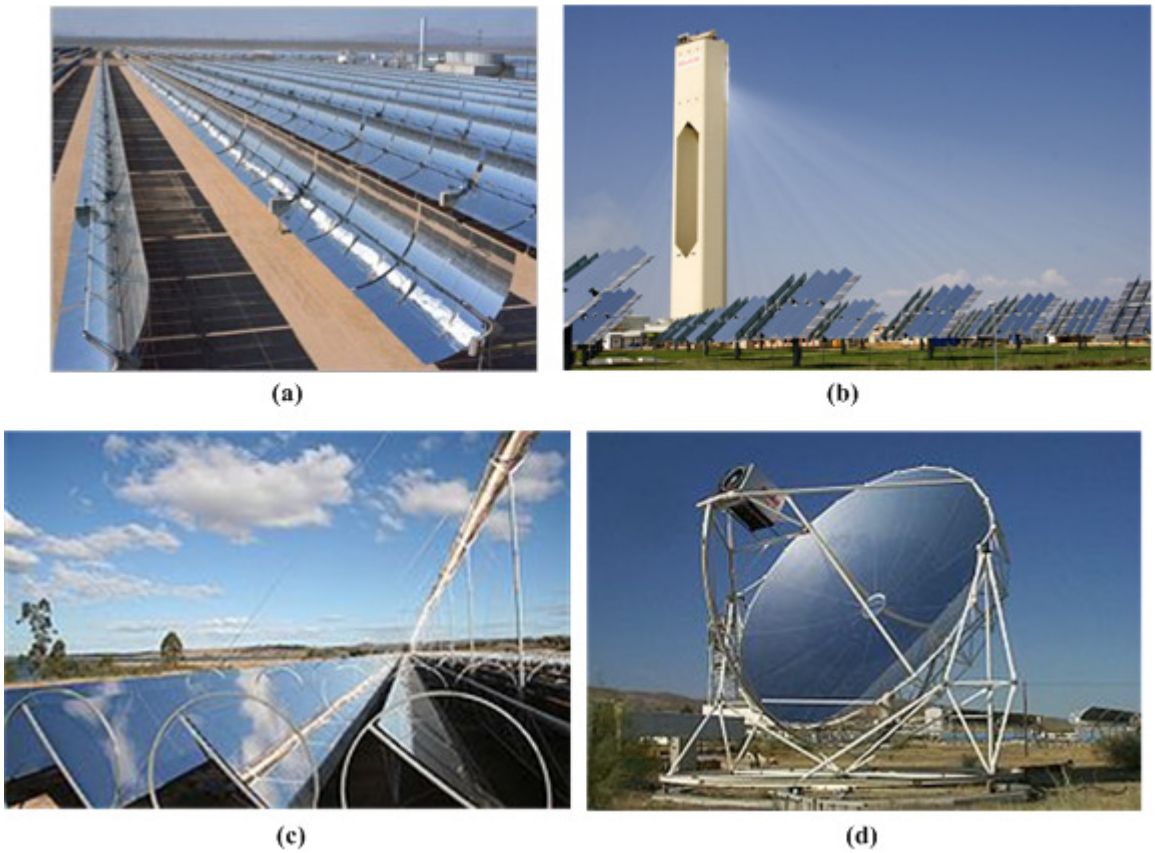

Figure 1.2: Photos of (a) Parabolic trough, (b) solar power tower, (c) Fresnel reflector, and (d) dish-Stirling CSP designs [3].

thermal energy from the sun to generate electricity. CSP technologies track the sun on either one or two axes, and mirrors are arranged to focus the sunlight in either line-focus concentrators or point-focus concentrators. The high temperatures achieved at the focal point of the concentrators is used to heat an intermediate heat exchanging fluid, which can either be used for thermal energy storage, boiling water (for steam turbine), or powering thermal engines. Four types of CSP are currently being developed: parabolic trough, power tower, linear Fresnel reflector, and dish-Stirling (DS) designs. Figure 1.2 displays a photo [3] of each type of system. Parabolic trough and linear Fresnel reflector designs use line-focus concentrators, track the sun on one axis, and boil water in a conventional steam turbine-driven generator, making their design resemble a conventional fossil-fueled thermal power plant. DS and power tower designs use point-focus concentrators and track the sun on two-axes, but only power tower designs use a conventional steam-turbine prime mover. DS systems use the concentrated sunlight to drive a closed-cycle, external heat engine known as a Stirling engine. Parabolic trough is the most mature of the CSP technologies, having 11 individual plants with a total generation capacity of 426 MW in the U.S. [2]. Table 1.1 gives various data comparing the four types of CSP. NREL maintains a database of information on current CSP projects in five countries: Algeria, Italy, Morocco, Spain, and the U.S. The generation capacity data shown in Table 1.1 comes from this database, but includes only data for the U.S. CSP projects in the U.S. that have been reported to NREL will amount to over 4500 MW of generating capacity by 2014, which significantly exceeds the U.S. Energy Information Administration's (EIA) 2010 Annual Energy Outlook (AEO) [1] estimate (shown in Fig. 1.1) of 862 MW by 2014. Cost data for CSP technologies varies substantially between sources, and a range of prices for each technology (if available) is given in Table 1.1, which shows the lowest and highest cost estimates given in the sources listed. DS technology has demonstrated the highest instantaneous and annual efficiency of the CSP technologies, where annual efficiency is defined as the ratio of the

Table 1.1: Cost, Generating Capacity, and Performance Data of CSP Technologies [2] [4] [5] [6]

	Current Installed Capacity in U.S. (MW)	Capacity in U.S. by 2014 (MW)	Largest Installation by 2014 (MW)	LCOE ($/MWh)	Annual Efficiency	Installed Cost ($/kW)
Trough	426	2032	280	50-110	13-17%	2805-4900
Tower	5	879	440	40-256.6	14-18%	2500-6800
Dish-Stirling	1.5	1601.5	850	60-400	20-26%	3000-8600
Fresnel Reflector	6.4	6.4	5	N/A	N/A	N/A

electric energy produced and incident solar energy supplied to the system over a year. The instantaneous efficiency varies during daily operation depending on operating conditions. DS systems, however, currently have higher costs, as shown in Table 1.1.

DS technology has demonstrated the highest sun-to-grid energy conversion efficiency [7] of any solar technology. Although DS technology is not as mature as the trough and tower type designs, the advantages of higher efficiency and potential for low-cost at mass production levels [8] makes the technology a significant competitor in both the CSP technology market and other renewable energy markets. The potential of DS technology is already being seen in the utility scale renewable energy markets, where the first large scale DS power plant, rated at 1.5 MW, came online in January, 2010 in Peoria, AZ [9]. More projects are in development with Southern California Edison, CPS Energy, and San Diego Gas & Electric for 1627 MW of solar power from DS solar power plants [9]. Therefore, DS technology is emerging as a prominent player in the renewable energy electricity markets, and is likely to see a growing number of plants integrated into the utility grid. The integration of large numbers of DS systems into the utility grid poses unique challenges, particularly related to the reliability and stability of the generators and the grid. Modeling of solar farms is important to understand the DS system's impact on

the grid and to anticipate potential problems and develop solutions; until recently these topics have received little attention in the literature. The research presented in this thesis covers the modeling and grid interconnection issues of a DS solar farm, starting with the model of a single 25 kW system.

1.3 System Overview

A diagram of a DS system with labeled components is shown in Fig. 1.3. The concentrator, power conversion unit (PCU), and all structural components track the sun on two-axes throughout the day. The concentrator consists of mirrors arranged in the shape of a paraboloid, and is designed such that the focal point of the mirrors is at the opening of the receiver. The concentrator is sized to ensure that for different irradiance levels, the thermal input energy from the concentrator does not exceed the thermal ratings of the PCU. Concentrator diameters range from 8 to 15 meters in DS systems currently being developed [8]. The receiver acts as a thermal interface between the concentrated sunlight and the PCU, which contains the Stirling engine. The receiver is usually shaped like a cylinder with an opening at one end to absorb the concentrated sunlight, which

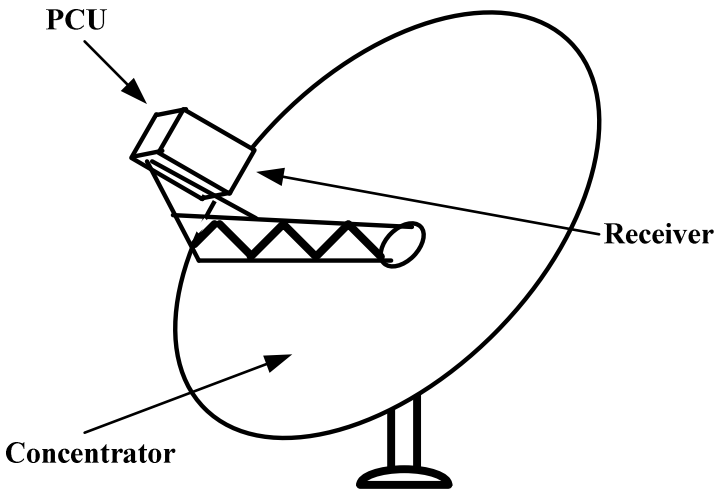

Figure 1.3: Sample dish-Stirling system with labeled components.

reduces convection heat losses. One of the Stirling engine heat exchangers, known as the heater (or absorber), consists of a series of tubes that pass through the receiver, where the engine working gas flows through and absorbs the heat from the concentrated sunlight. The working gas is expanded and compressed, supplying the work for a piston-crankshaft drive mechanism. The Stirling engine shaft is typically coupled to a cage rotor induction machine, which is used as the generator, and is also contained within the PCU.

Several variations in DS system designs exist, particularly in the Stirling engines. In general, two types of Stirling engines are discussed in the literature [10]: free-piston Stirling engines and kinematic Stirling engines. Free-piston engines are distinguished from kinematic Stirling engines by the lack of a traditional crankshaft drive mechanism. Instead, a linear alternator is used, containing a stationary coil of wire wrapped around the cylinder of a piston, and the piston contains some magnetic material, thereby inducing voltage in the stationary coil as the piston moves through the cylinder. Kinematic Stirling engines drive conventional generators, usually induction machines in grid-connected applications. Use of synchronous machines has been reported, but only in stand-alone water pumping applications [8]. The power output can be controlled in Stirling engines by either varying the working gas pressure or varying the stroke length of the pistons. Contrary to conventional steam generation, the Stirling engine/generator shaft speed is not controlled to a fixed value under normal operating conditions. The shaft speed is allowed to vary over a narrow band for changing irradiance, but remains below the slip (with respect to grid frequency) corresponding to the pull-out torque of the generator. However, during grid fault conditions, the speed must be controlled to protect the system from damage resulting from sharp increases in speed, a topic which is discussed in more detail in Chapter 3.

Two types of receivers currently exist in DS systems: direct illuminated receivers (DIR) and indirect illuminated receivers (IIR) [10]. In DIR, the concentrated sunlight is directly applied to the Stirling engine heater, whereas, in the IIR, an intermediate heat

exchanging fluid is used, usually molten salt. The molten salt condenses on the engine heater, where the heat is then absorbed by the Stirling engine, and the molten salt is re-circulated in the receiver. The IIR can achieve more uniform temperature distribution than the DIR, but is a more complex design.

DS systems using DIR and kinematic Stirling engines with variable pressure control are the most common designs [8] [10], and are the focus of this thesis. Reasons for this design trend include the simplicity, cost, and the lack of maturity in other technologies, even though higher performance may be achieved from different designs.

1.4 Dish-Stirling Background

The Stirling engine was invented in 1816 by the Scottish clergyman Robert Stirling [10]. Stirling's design proved to be a quieter and safer alternative to the steam engine of the day, and grew quite popular throughout the rest of the 19th century. However, due to material limitations and the invention of the internal combustion engine and the electric machine, development of the engine slowed considerably at the turn of the century [11]. Renewed interest in the Stirling engine occurred during the mid 20th century due to material advancements and the Stirling engine's potential for high efficiency. Development of Stirling engines included applications in transportation, generators, and refrigeration [11]. In the late 1970's, Jet Propulsion Laboratory began designing and constructing the first DS system with funding from the U.S. Department of Energy [12]. Four companies are currently developing DS systems, including Science Applications International Corp. (SAIC) with partner STM Power, Inc., Stirling Energy Systems (SES), and WGAssociates in the United States, and Schlaich-Bergermann and Partner (SBP) are leading the Eurodish project in Europe [8]. SES, with partner Tessera Solar, constructed the first commercial scale DS solar farm in Peoria, AZ, which came online in January 2010 as a 1.5 MW plant. The demonstration plant includes 60 DS units at 25 kW each [9].

1.5 Literature Review

Literature on dish-Stirling systems is limited and scattered, while literature on the individual components, particularly the Stirling engine, is quite abundant. However, literature that investigates the application of Stirling engines with solar concentrators is rather scarce and scattered.

1.5.1 Stirling Engines

The ideal Stirling cycle, which has a pressure-volume diagram shown in Fig. 1.4, provides a simple introduction to the working gas cycle inside the engine. The cycle includes two constant-volume processes and two isothermal processes. Transition 1-2 is an isothermal expansion of the working gas, transition 2-3 is a constant-volume heat removal from the working gas, transition 3-4 is an isothermal compression of the working gas, and transition 4-1 is a constant-volume heat addition to the working gas. The efficiency of the ideal Stirling cycle is theoretically equivalent to the Carnot cycle [13], given by

$$\eta = 1 - \frac{T_3}{T_1} \tag{1.1}$$

where T_1 and T_3 refer to the temperatures at points 1 and 3 of the ideal Stirling cycle

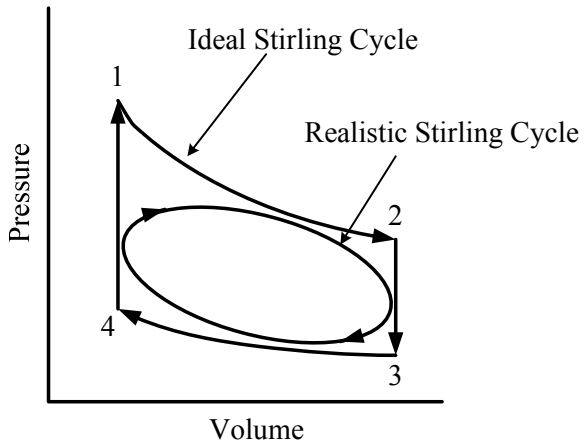

Figure 1.4: Stirling cycle p-v diagram.

shown in Fig. 1.4. Actual operation of the Stirling engine differs greatly from the characteristics of the ideal cycle, due in part to the sinusoidal nature of the volume variations in the engine. A more realistic pressure-volume diagram of the Stirling cycle is like an ellipse as shown in Fig. 1.4.

A broad review of the Stirling engine, including the history, applications, mathematical analysis, configurations, and design, can be found in [11] and [13]. Early mathematical analyses of Stirling engines began in 1871 with the publication by Gustav Schmidt [11], but made unrealistic assumptions, including an analysis that was largely dependent on the principles of the ideal Stirling cycle. Nevertheless, Stirling engine mathematical analyses during the first half of the twentieth century were largely based on the analysis of Schmidt. A nodal analysis method is discussed in [14] [15] [16], where the engine compartments are divided into finite length segments, and an energy and mass balance performed on each segment. The assumptions of Schmidt's analyses were no longer applied in the nodal analysis method, giving a more realistic model for the engine. An ideal adiabatic analysis is discussed in [17] and [18], with the primary assumption being adiabatic expansion and compression of the working gas. Stirling engine analysis methods range significantly in complexity, with Schmidt's analysis generally being the most simple, having a closed form solution. Variations of the nodal analysis method tend to be the most complex, requiring numerical integration solution techniques and extensive engine operation and dimension data.

1.5.2 Receivers

A thermal energy storage receiver design is proposed in [19], in which the thermal energy is stored in the mass of the receiver material; a mathematical analysis of how the temperature of the receiver varies with time and axially along the receiver length is provided. A detailed analysis of the conduction, radiation, and convection losses in an IIR is provided in [20] [21]. Modeling techniques of the Eurodish DS system are given

in [22], where a nodal analysis is performed on different sections of the receiver, and a non-uniform solar flux on the receiver is taken into account.

1.5.3 Dish-Stirling Performance Reports, Design, Modeling

An overview of several different DS designs is given in [10], including details regarding receiver, concentrator, and Stirling engine dimensions and operating characteristics. An explanation of the starting sequence of the DS system is given in [12], where the generator acts as a motor to bring the Stirling engine to operating speed. A diagram of the pressure control system is provided, along with plots of the DS system parameters on a cloudy day and a waterfall chart listing the various losses in the entire DS system. Detailed and lengthy reports of the Vanguard system performance are given in [23] and [24], which include valuable information regarding the engine pressure, temperature, speed, and power output for varying irradiance. Steady state and transient plots are provided. Modeling techniques of the receiver and Stirling engine in the Eurodish system are given in [22] with a focus on the steady state performance comparison with simulation model results for power output versus irradiance. Grid interconnection of DS systems is discussed in [25], particularly on issues related to low voltage ride through, reactive power compensation, and power factor correction.

1.5.4 Control Systems

Control systems for Stirling engines in constant and variable speed applications are described in [26], where the focus is on temperature control of the receiver for varying irradiance conditions, and provides test results of the gas pressure and receiver temperature for a Stirling engine using external combustion to simulate heat from solar irradiance. External combustion of fossil fuel is used to heat the Stirling engine working gas, and varying irradiance levels are simulated by varying the amount of fuel added in the combustion. Similar descriptions of the temperature and pressure control systems described in [26] can also be found in [12], [23], and [24]. A comparison of the variable

swashplate angle and variable pressure method for controlling power output is given in [27].

1.6 Summary

Growth of solar power generating capacity is inevitable due to both an increase in the world's energy needs and the need for cleaner sources of energy. CSP can meet the new clean energy needs for utility scale power generation at a potentially cost competitive rate with conventional power generation. DS technology has demonstrated the highest energy conversion efficiency of the CSP technologies, and is the focus of the research presented in this thesis. Because DS systems are relatively new to the commercial electric power sector, literature on DS systems for electric power generation is rather scarce. Therefore, the research presented in this thesis attempts to fill in the gaps between the well-documented thermodynamic analysis of the various DS components and the electric power issues that arise in the grid interconnection of DS systems. Portions of the research presented in this thesis have been accepted for publication, and are given in [28], [29], and [30].

Chapter 2 focuses on the DS system model, which includes integration of the concentrator, receiver, Stirling engine, and induction generator sub-models. The Stirling engine requires modeling of the internal gas dynamics and internal heat exchangers, along with the mechanical characteristics of the engine. A method for simulation of the DS model is provided along with steady-state simulation results of key engine parameters.

The DS control systems are discussed in Chapter 3. The primary control objectives are to maintain the receiver temperature within safe operating limits and to prevent over-speeding of the engine/generator shaft during grid faults, both of which are controlled by varying the engine working gas pressure. Block diagrams of the

temperature, pressure, and over-speed control systems are given, along with a linearized model of the Stirling engine and pressure control system for controller tuning.

In Chapter 4, the DS system is connected in a single-machine infinite bus (SMIB) system, and simulation results for both steady state and transient operation are given. Potential grid-interconnection requirements are discussed, and reactive power compensation required to meet such requirements is given. Simulation results for the DS system under a grid-fault are used to evaluate the performance of the control systems discussed in Chapter 3.

Several case studies for connecting a DS solar farm into a small IEEE 12-bus power network are given in Chapter 5 and evaluated under irradiance and grid transients. Since a DS solar farm consists of thousands of individual DS units, different methods for modeling a solar farm are considered in order to reduce simulation time and complexity. The simplest method assumes uniform solar irradiance over the entire solar farm area and neglects inter-machine dynamics, which results in simply scaling the generator ratings and parameters from 25 kW to an equivalent MW rated machine in order to account for multiple generators. The most complex modeling method simulates each 25 kW generator system individually, taking into account possible variations in irradiance between neighboring DS systems. Grid interconnection issues are discussed, including the low voltage ride through (LVRT) capability of the solar farm and power factor correction requirements.

CHAPTER 2

COMPONENT MODELS

2.1 Introduction

Component models for the concentrator, receiver, and Stirling engine of a dish-Stirling (DS) system are presented in this chapter. The dimensions and operating data of several DS systems are provided in [10], and can be used to develop models of a particular DS design. The dimensions of the various system components, model gains, working gas properties, and system ratings used in simulations are provided in Appendix A.

2.2 Concentrator

The concentrator focuses the direct normal irradiance (DNI) onto the receiver, where the heat is used in the energy conversion process. The key parameters in analyzing the operation of the concentrator are the dish aperture diameter d_{con} (m), mirror reflectivity η_m, and irradiance I (W/m^2). With the assumption of perfect sunlight tracking, the rate of heat transfer to the receiver from the concentrator can be approximated by

$$DQ_I = \pi\left(\frac{d_{con}}{2}\right)^2 \eta_m I = K_C I \tag{2.1}$$

where D is the derivative operator with respect to time, Q_I is the concentrated solar energy (J), and K_C is defined as the concentrator gain (m^2). Although the mirror reflectivity is assumed to be constant, in practice the reflectivity will change over time, with dust and debris collecting on the mirrors reducing the reflectivity and requiring periodic cleaning.

2.3 Receiver

The receiver is a cylindrical mass that serves as the interface between the concentrator and the Stirling engine. The receiver is designed to maximize the amount of heat transferred to the Stirling engine and minimize the thermal losses. Inside the receiver at the base lies the absorber, which consists of a mesh of tubes that carry the Stirling engine working gas. This gas flows through the mesh of tubes to absorb the heat inside the receiver to power the Stirling engine. The receiver introduces losses in the system due to thermal radiation, reflection, convective heat transfer into the atmosphere, and conduction through the receiver material [22].

Critical to the receiver operation is the temperature of the absorber. The temperature should be maintained as high as possible to maximize the efficiency of the Stirling engine, but should not exceed the thermal limits of the receiver/absorber material. Thus, the absorber temperature is a major control variable. An energy balance on the absorber yields the relation

$$\rho\, c_p V D T_h = DQ_I - DQ_L - DQ_h \tag{2.2}$$

where ρ is the absorber material density (kg/m^3), c_p is the specific heat capacity of the absorber material (J/kg*K), V is the absorber material volume (m^3), T_h is the absorber temperature (K), Q_L is the heat loss of the absorber (J), and Q_h is the heat transferred to the Stirling engine (J). It is evident from (2.2) that the absorber temperature can be controlled by controlling the rate of heat transfer to the Stirling engine DQ_h. Taking the Laplace transform of (2.2) and rearranging the terms gives

$$T_h = \frac{1}{\rho c_p V}\left[\frac{DQ_I - DQ_L - DQ_h}{s}\right] = \frac{K_R}{s}\left[DQ_I - DQ_L - DQ_h\right] \tag{2.3}$$

where K_R is defined as the absorber gain (K/J). The losses in the absorber can be defined in terms of an average loss heat transfer coefficient h (W/m^2*K) [19], given by

$$DQ_L = hA(T_{avg} - T_a) = K_L(T_{avg} - T_a) \tag{2.4}$$

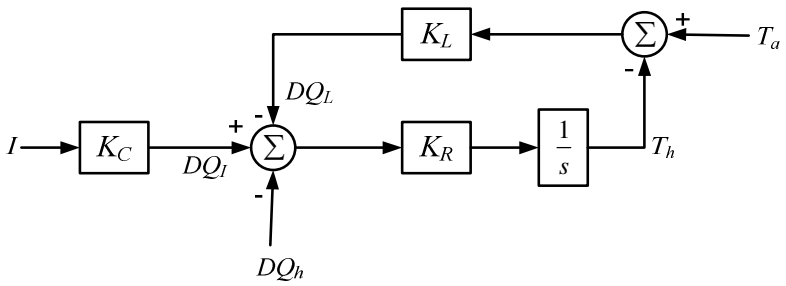

Figure 2.1: Concentrator and receiver block diagram.

where A is a constant proportional to the receiver dimensions (m^2), T_{avg} is a temperature that characterizes the heat loss in the absorber (K), T_a is the ambient temperature (K), and K_L is defined as the gain representing the rate of heat loss (W/K). T_{avg} is assumed to be equal to the absorber temperature, making the thermal losses in the receiver proportional to the difference between the receiver temperature and ambient temperature. Thus, from (2.3) and (2.4), the block diagram of the absorber is given in Fig. 2.1. The rate of heat transferred to the Stirling engine DQ_h controls the absorber temperature, and is calculated using the methods of the next section.

2.4 Stirling Engine

A simplified diagram of a two-cylinder Stirling engine is shown in Fig. 2.2. The engine is a closed-cycle external heat engine with a working gas, usually hydrogen or helium, contained within the engine. By definition, the working gas within a closed-cycle engine never leaves the engine. Therefore, the control valve shown in Fig. 2.2 is normally closed. Only for a change in the DS operating point does the control valve open, a topic which is discussed in detail in the next chapter. Heat exchangers alternately heat and cool the working gas, causing expansion and compression within the working spaces of the engine, where the work done in the expansion of the gas is used to drive a piston-crankshaft drive mechanism. The engine contains three heat exchangers, known as the heater, cooler, and regenerator. "Heater" is the general term used in Stirling engine literature, but represents the same mesh of tubes discussed in the previous sections known

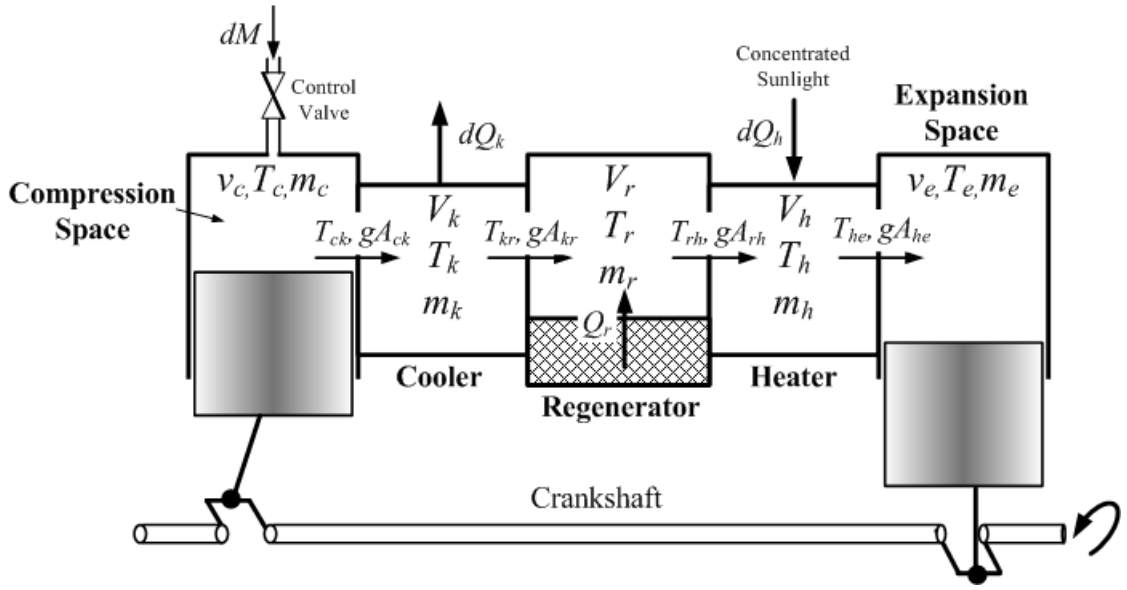

Figure 2.2: Heat exchangers and working spaces in a Stirling engine, with labels for the various gas parameters in each compartment.

as the absorber. The heat exchanger elements shown in Fig. 2.2 are simply represented as one volume equal to the sum total of the volumes of all the tubes inside the corresponding section. The working gas flows back and forth through the tubes of the heater, absorbing heat to power the Stirling engine. The regenerator is a dense wire mesh intended to recapture some of the heat stored in the working gas before entering the cooler, where it will otherwise be ejected into the atmosphere. The cooler rejects excess heat to the atmosphere by various means, which can include forced air convection or water cooling. The working spaces within the engine are known as the expansion and compression spaces. The working space volumes are directly connected to the crankshaft mechanism, thus their instantaneous volumes depend on the crankshaft angle, or shaft rotational speed.

Stirling engine analysis and simulation rely on knowing the instantaneous pressure, temperature, mass, and volumes of the various spaces within the engine. An ideal adiabatic model developed by Urieli [17] provides a means of modeling the various engine parameters, with the primary assumption being adiabatic expansion and compression of the working gas in the working spaces. The model is developed by

performing an energy balance on each of the heat exchanger and working space volumes. A derivation of the ideal adiabatic model equation set can be found in [18], but assumes a constant mass of working gas within the engine, constant heater temperature, and constant shaft speed. In DS applications, the engine working gas pressure is varied by changing the amount of working gas within the engine via a control valve similar to that shown in Fig. 2.2, and thus the assumption of constant mass is no longer valid. In addition, the heater temperature and shaft speed vary depending on the instantaneous solar irradiance and pressure of the working gas. Therefore, a similar derivation of an ideal adiabatic model equation set given in [18] is provided here, without these assumptions. In addition, the equation set developed here for the Stirling engine is based on the course notes of Urieli on Stirling engines [31], but modified to account for the non-constant quantity of working gas mass, non-constant heater temperature, and non-constant shaft speed.

Before analyzing the various engine compartments, the equations of the generalized engine compartment shown in Fig. 2.3 are developed. Using the First Law of Thermodynamics for an open system, an energy balance on the compartment gives the following relationship [18]:

$$dQ + c_p\left(T_i gA_i - T_o gA_o\right) = dW + c_v d\left(mT\right) \tag{2.5}$$

where d is the derivative with respect to the engine crankshaft angle ϕ, Q is heat (J), c_p is the specific heat capacity at constant pressure of the gas (J/kg*K), T_i and T_o are the temperature of the gas entering and exiting the cell (K), gA_i and gA_o are the mass flow rates of the gas entering and exiting the cell (kg/rad), W is the work done by the cell (J), c_v is the specific heat capacity of the gas at constant volume (J/kg*K), m is the mass of gas within the cell (kg), and T is the temperature of the gas within the cell (K). Assuming the working gas behaves as an ideal gas, the relationship between the pressure p (Pa), volume v (m^3), mass m (kg), and temperature T (K) of the working gas is given by

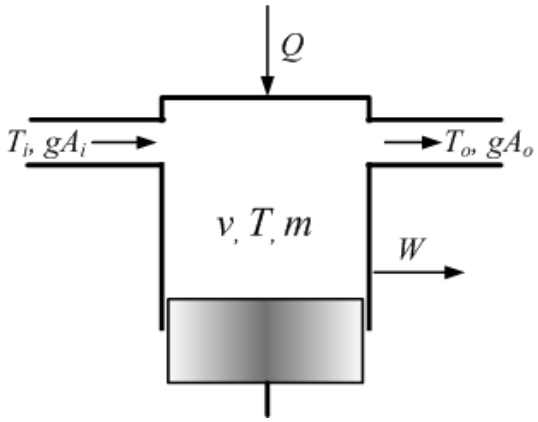

Figure 2.3: Generalized engine compartment.

$$pv = mRT \tag{2.6}$$

where R is the gas constant (J/kg*K). Taking the natural logarithm of each side of (2.6) and differentiating, the differential form of the ideal gas equation becomes

$$\frac{dp}{p} + \frac{dv}{v} = \frac{dm}{m} + \frac{dT}{T} \tag{2.7}$$

The generalized Stirling engine compartment has a variable volume, a heat transfer, work output, and both a mass flow inlet and outlet. The various Stirling engine compartments of Fig. 2.2 are simplified versions of the generalized compartment of Fig. 2.3, and an analysis of each of the various engine compartments is presented below.

2.4.1 Heat Exchanger Analysis

The heat exchangers in the Stirling engine, shown in Fig. 2.2 as the heater, cooler, and regenerator, have a constant volume V, thus the work term dW in (2.5) is equal to zero. The steady-state temperature distribution of the working gas in the various compartments is illustrated in Fig. 2.4. The heat exchangers' gas temperatures are assumed to be uniform throughout the control volume and equal to the material wall temperature. The cooler temperature is assumed to remain constant, but the heater temperature can vary with both solar irradiance and the engine working gas pressure. The effective regenerator temperature T_r [31] is defined in terms of the heater and cooler

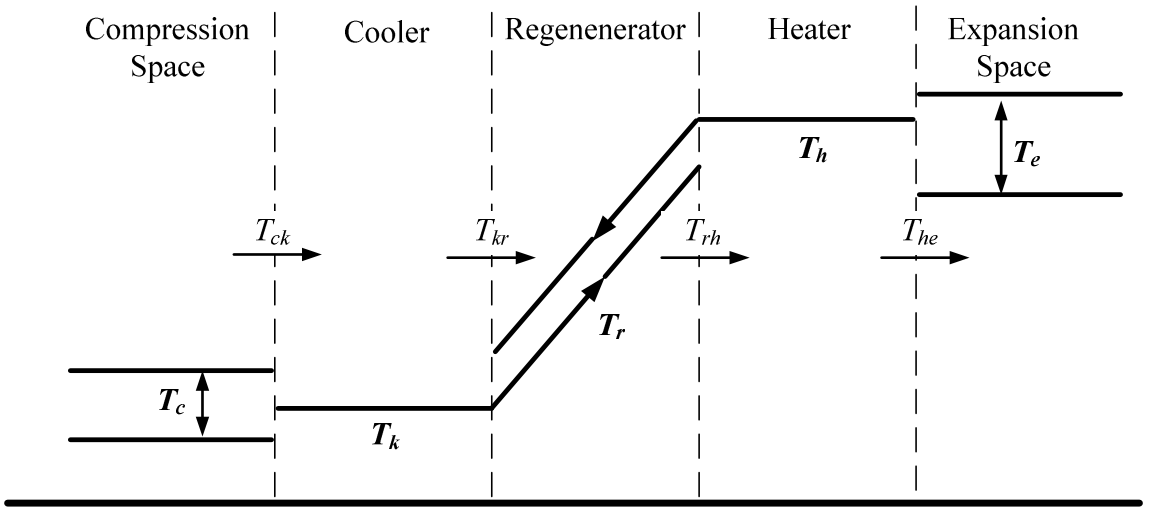

Figure 2.4: Working gas temperature distribution throughout the five engine compartments.

temperatures T_h and T_k, given by

$$T_r = \frac{T_h - T_k}{\ln(T_h / T_k)} \tag{2.8}$$

where all temperatures are in units of Kelvin. Since the heater temperature varies, the regenerator temperature will vary as well. Thus the rate of change of the regenerator temperature in terms of the heater and cooler temperature can be found by differentiating (2.8) with respect to the crank angle ϕ, and is given by

$$dT_r = \frac{dT_h \ln(T_h / T_k) - dT_h + (T_k / T_h) dT_h}{\ln(T_h / T_k)^2} \tag{2.9}$$

The interface temperatures between the Stirling engine compartments depend on the direction of mass flow, presenting a discontinuity in the Stirling engine gas model. Referring to the arbitrarily chosen direction of mass flow in Figs. 2.2 and 2.4, the conditional statements describing the interface temperatures [31] are given by

$$\begin{aligned}
&if \quad gA_{ck} > 0, \quad then \quad T_{ck} = T_c; \quad else, \quad T_{ck} = T_k \\
&if \quad gA_{kr} > 0, \quad then \quad T_{kr} = T_k; \quad else, \quad T_{kr} = T_{h2} \\
&if \quad gA_{rh} > 0, \quad then \quad T_{rh} = T_{k1}; \quad else, \quad T_{rh} = T_h \\
&if \quad gA_{he} > 0, \quad then \quad T_{he} = T_h; \quad else, \quad T_{he} = T_e
\end{aligned} \tag{2.10}$$

where the various interface temperatures and mass flow rates are labeled in Figs. 2.2, 2.4,

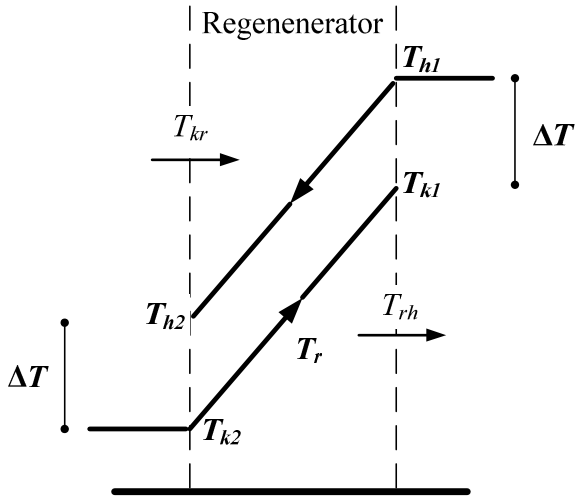

Figure 2.5: Regenerator temperature distribution and conditional interface temperatures.

and 2.5. Fig. 2.5 shows a detailed view of the regenerator temperature distribution. In an ideal regenerator, the interface temperatures T_{kr} and T_{rh} are equal to the cooler and heater temperatures, respectively, regardless of the direction of mass flow. However, in practice, not all of the heat absorbed by the regenerator (when the gas passes from the heater to the regenerator) will be delivered back to the heater (when the gas passes from the regenerator to the heater). Thus, the temperature of the gas entering the regenerator (from the heater) will be higher than the temperature of the gas re-entering the heater (from the regenerator) due to thermal losses and non-idealities of the regenerator. The regenerator performance is quantified using a regenerator effectiveness parameter [31], given by

$$\varepsilon = \frac{1}{\left(1 + \frac{\Delta T}{T_{h1} - T_{h2}}\right)} \tag{2.11}$$

where the various terms in (2.11) are labeled in Fig. 2.5. ΔT is assumed to be proportional to the difference in the heater and cooler temperature, resulting in a decrease in regenerator effectiveness as the difference in temperature between the heater and cooler increases.

Taking into account the constant volume of the heat exchangers, the change of mass in the heat exchangers is found from (2.7), given by

$$\begin{aligned} dm_h &= m_h \frac{dp}{p} - m_h \frac{dT_h}{T_h} \\ dm_r &= m_r \frac{dp}{p} - m_r \frac{dT_r}{T_r} \\ dm_k &= m_k \frac{dp}{p} \end{aligned} \tag{2.12}$$

where the various masses are labeled in Fig. 2.2.

Finally, an energy balance on the heat exchangers can be found from (2.5) after eliminating the *dW* term, substituting the ideal gas equation of (2.6), and solving the equation in terms of the heat transfer rate, given by

$$\begin{aligned} dQ_h &= \frac{V_h dp c_V}{R} - c_P (T_{rh} g A_{rh} - T_{he} g A_{he}) \\ dQ_r &= \frac{V_r dp c_V}{R} - c_P (T_{kr} g A_{kr} - T_{rh} g A_{rh}) \\ dQ_k &= \frac{V_k dp c_V}{R} - c_P (T_{ck} g A_{ck} - T_{kr} g A_{kr}) \end{aligned} \tag{2.13}$$

where V_h, V_r, *and* V_k are the constant heat exchanger volumes (m^3) and Q_h, Q_r, and Q_k are the amount of heat in the heat exchangers (J), as labeled in Fig. 2.2.

2.4.2 Working Space Analysis

The temperature distribution shown in Fig. 2.4 represents the steady-state temperature of the working gas in each compartment of the engine, indicating that the expansion and compression space temperatures have periodic oscillations in steady state, while the heat exchanger temperatures remain relatively constant in steady state. The relationship between the working space volumes v_e and v_c and the crank angle ϕ [16] is given by

$$\begin{aligned} v_c &= V_{dc} + 0.5V_s\left[1+\cos(\phi-\alpha_c)\right] \\ v_e &= V_{de} + 0.5V_s\left[1+\cos(\phi-\alpha_e)\right] \\ dv_c &= -0.5V_s\sin(\phi-\alpha_c) \\ dv_e &= -0.5V_s\sin(\phi-\alpha_e) \end{aligned} \tag{2.14}$$

where V_{dc} and V_{de} are the dead space volumes of the expansion and compression spaces (m^3), V_s is the cylinder swept volume (m^3), and $\alpha_{c,e}$ is the displacement angle of the expansion/compression space (rad). The working spaces are assumed to operate adiabatically ($dQ = 0$). The work produced by the working spaces is a result of the engine gas pressure acting on the pistons. Applying these operating principles to (2.5), an energy balance on the compression space volume shown in Fig. 2.2 is given by

$$c_p\left(T_k dM - T_{ck} gA_{ck}\right) = pdv_c + c_v d\left(m_c T_c\right) \tag{2.15}$$

where the gas entering the compression space from the control valve, dM (kg/rad), is assumed to be at the cooler temperature T_k. The mass flows into/out of the Stirling engine compartments is described using

$$\begin{aligned} gA_{ck} &= dM - dm_c \\ gA_{kr} &= gA_{ck} - dm_k \\ gA_{he} &= dm_e \\ gA_{rh} &= gA_{he} + dm_h \end{aligned} \tag{2.16}$$

The compression space mass can be found by applying the ideal gas equation of (2.6) and the first equation of (2.16) to (2.15), and solving for dm_c gives

$$dm_c = \frac{pdv_c + v_c dp/\gamma}{RT_{ck}} - \frac{\left(T_k - T_{ck}\right)dM}{T_{ck}} \tag{2.17}$$

where γ is the ratio of specific heats (c_p/c_v). Similarly, the change in expansion space mass dm_e is given as [17] [18]

$$dm_e = \frac{pdv_e + v_e dp/\gamma}{RT_{he}} \tag{2.18}$$

In steady state, dM is zero, and thus the relationships describing the compression and expansion space masses in (2.17) and (2.18) are similar. The temperature of the working

gas in the working space volumes is found from (2.7), and, after rearranging terms, gives the relationship

$$\begin{aligned} dT_c &= T_c\left(\frac{dp}{p}+\frac{dv_c}{v_c}-\frac{dm_c}{m_c}\right) \\ dT_e &= T_e\left(\frac{dp}{p}+\frac{dv_e}{v_e}-\frac{dm_e}{m_e}\right) \end{aligned} \tag{2.19}$$

2.4.3 Engine Pressure

Using the ideal gas equation, and neglecting pressure drops across the various engine compartments, the pressure of the gas inside the Stirling engine of Fig. 2.2 is given by [31]

$$p = \frac{MR}{\left(v_c/T_c + V_k/T_k + V_r/T_r + V_h/T_h + v_e/T_e\right)} \tag{2.20}$$

where M is the total quantity of gas inside the engine (kg). Referring to the diagram of Fig. 2.2, the total mass of the Stirling engine working gas is given by

$$M = m_c + m_e + m_h + m_k + m_r \tag{2.21}$$

Differentiating (2.21), the mass equation becomes

$$dM = dm_c + dm_e + dm_h + dm_k + dm_r \tag{2.22}$$

Applying (2.12) to (2.22), the mass equation becomes

$$dM = dm_c + dm_e + dp\left(\frac{m_k}{p}+\frac{m_h}{p}+\frac{m_r}{p}\right) - m_h\frac{dT_h}{T_h} - m_r\frac{dT_r}{T_r} \tag{2.23}$$

Using the ideal gas equation of (2.6), (2.23) can be rewritten as

$$dM = dm_c + dm_e + \frac{dp}{R}\left(\frac{V_k}{T_k}+\frac{V_h}{T_h}+\frac{V_r}{T_r}\right) - \frac{pV_h}{R}\frac{dT_h}{T_h^2} - \frac{pV_r}{R}\frac{dT_r}{T_r^2} \tag{2.24}$$

Substituting the compression and expansion space mass equations of (2.17) and (2.18) into (2.24) and rearranging the terms gives the pressure derivative to be

$$dp = \frac{\gamma R dM\left(T_k/T_{ck}\right) - \gamma p\left[\left(dv_c/T_{ck}\right) + \left(dv_e/T_{he}\right) - V_r dT_r/T_r^2 - V_h dT_h/T_h^2\right]}{\left[v_c/T_{ck} + \gamma\left(V_k/T_k + V_r/T_r + V_h/T_h\right) + v_e/T_{he}\right]} \tag{2.25}$$

2.4.4 Mechanical Equations

The torque developed by the Stirling engine is a result of the pressure acting on the pistons, a relationship given by [14]

$$\tau = p\left(dv_c + dv_e\right) \tag{2.26}$$

The rotational equation of motion of the Stirling engine shaft is given by

$$\tau = JD\omega + F\omega + \tau_{elec} \tag{2.27}$$

where J is the moment of inertia (kg*m^2), ω is the engine/generator shaft rotational speed (rad/s), F is the mechanical damping constant (kg*m^2/s), and τ_{elec} is the electric load torque.

2.4.5 Modeled Engine

A four cylinder Stirling engine, based on the Siemens [11] or coaxial double-acting [13] configuration, is simulated, with the cylinder configuration and drive mechanism shown in Fig. 2.6(a). The engine is divided into four quadrants, each quadrant having its own set of heat exchangers, as shown in Fig. 2.6(b). Assuming no leakage past the pistons, the working gas in each quadrant is isolated from the neighboring quadrant. Therefore, each piston is connected to the expansion space of one quadrant and the compression space of the neighboring quadrant. Each quadrant is assumed to be identical in both dimensions and working gas quantity. Therefore, the only difference in operation between the four quadrants is a result of the displacement angles α given in (2.14). The displacement angle is set to 90^o for the four cylinder engine, resulting in a 90^o phase shift between the sinusoidal volume variations in the four expansions spaces and the four compression spaces. The 90^o phase shift in volume variations also causes a 90^o phase shift in the variations in pressure, temperature, mass flows, etc. between the four quadrants.

Each quadrant is modeled by the ideal adiabatic analysis described above. The

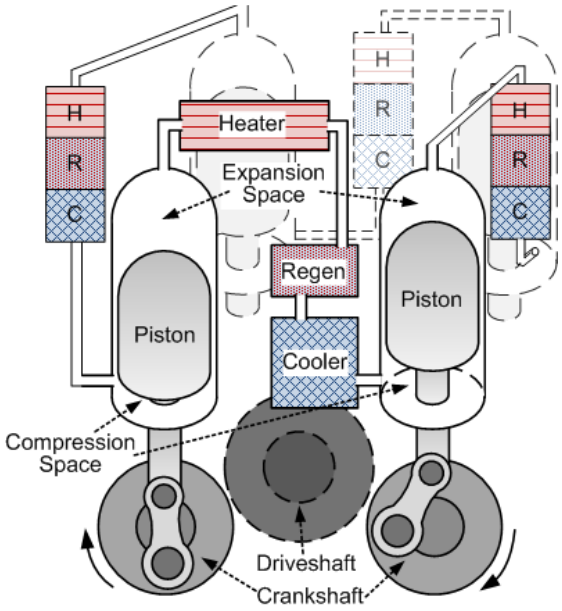

(a)

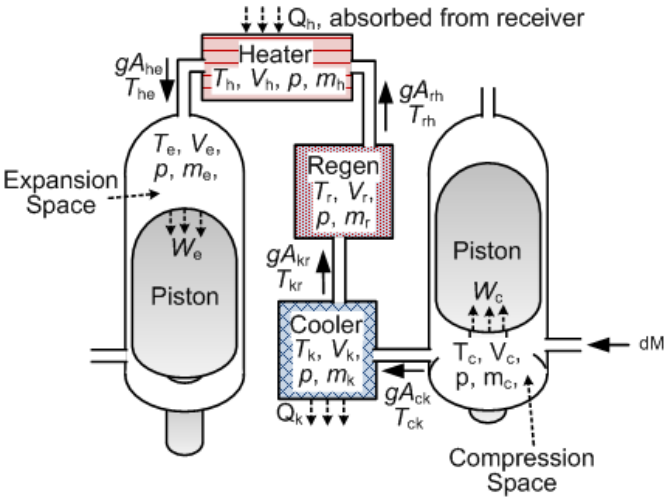

(b)

Figure 2.6: (a) Modeled 4-cylinder engine and (b) one quadrant of the four cylinder engine.

mechanical torque is thus a result of the four quadrant pressures acting on the pistons. Modifying (2.26) for the four cylinder engine, the mechanical torque developed by the Stirling engine is given by

$$\tau = p_1\left(dv_{c1} + dv_{e1}\right) + p_2\left(dv_{c2} + dv_{e2}\right) + p_3\left(dv_{c3} + dv_{e3}\right) + p_4\left(dv_{c4} + dv_{e4}\right) \qquad (2.28)$$

where the numerical subscript indicates the corresponding quadrant number.

Results of the pressure, temperature, compression space mass, and torque for

several revolutions of the crankshaft are shown in Fig. 2.7. Set points for the simulation are an irradiance I of 1000 W/m^2 and an absorber/heater temperature T_h of 993 degrees Kelvin. The sinusoidal volume variations in the compression and expansion spaces cause periodic oscillations in the engine parameters.

2.4.6 Simulation Strategy

Simulation of the Stirling engine requires calculation of the various working gas parameters at each increment of the simulation time step. The engine working gas parameters are calculated using the ideal adiabatic analysis discussed above, with solutions for the volume, pressure, mass, and their derivatives, determined analytically, while calculations of the expansion and compression space temperatures are determined

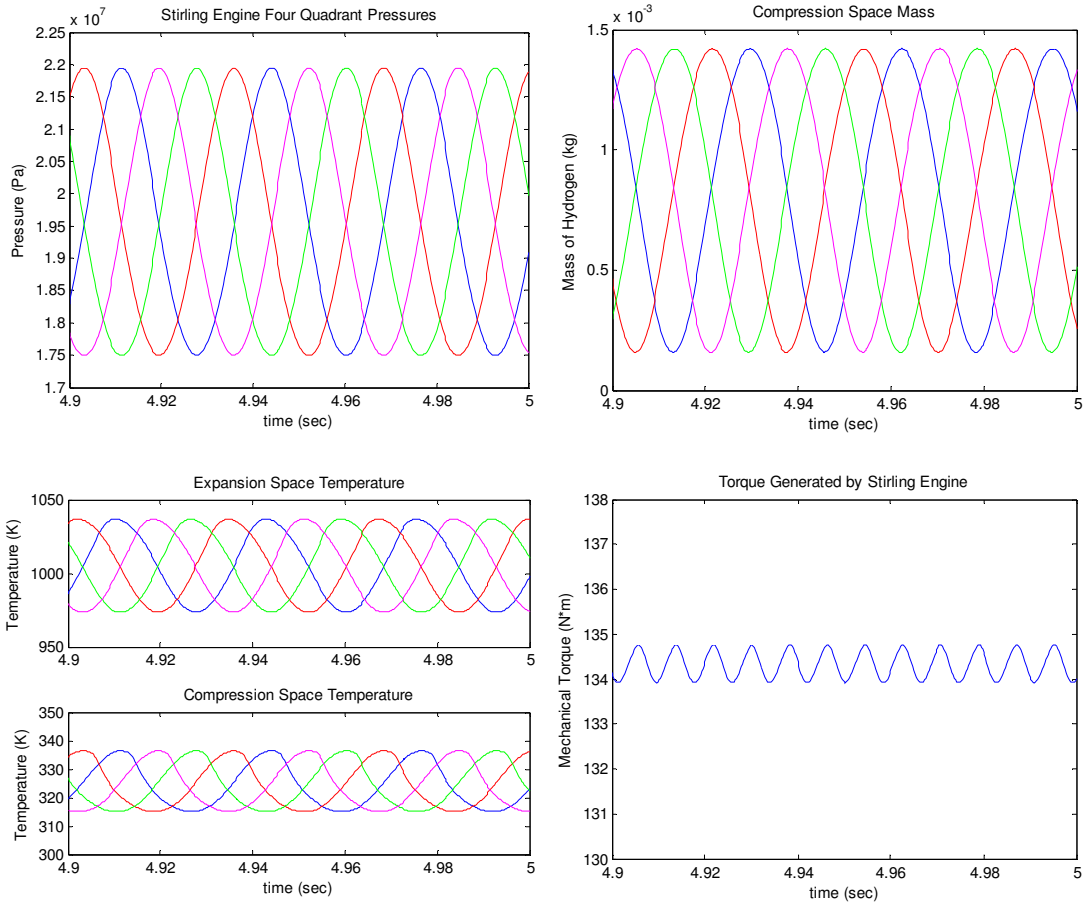

Figure 2.7: Simulation results for various Stirling engine parameters in steady state.

using numerical integration. Numerical integration of the expansion and compression space temperature differential equations for *each* of the four quadrants is required, totaling eight differential equations for the Stirling engine. The flow diagram for simulation of the Stirling engine parameters is shown in Fig. 2.8. For visual simplicity, the numerical subscript indicating the quadrant number of the various gas parameters is left off in the flow diagram of Fig. 2.8, however, it is implied that the parameters in every quadrant are calculated. During initialization of the simulation, the engine dimensions, working gas properties, and constant cooler temperature T_k must be specified. Initial conditions must be given for the crank angle ϕ, conditional interface temperatures T_{ck} and T_{he}, heater temperature T_h, total working gas mass M, and engine/generator speed ω. The initial derivates dT_h and dM are set to zero. The initial conditions for T_{ck} and T_{he} are set to the cooler and heater temperatures, respectively. The differential equations' solution is formulated as a quasi-steady initial value problem, where the heater temperature change rate dT_h, the shaft speed ω, and total engine mass change rate dM are assumed to remain constant over an integration cycle. The numerical integration technique used is the fourth order Runge-Kutta (RK4) method, with the initial value problem set up as

$$d\boldsymbol{Y} = \boldsymbol{F}\left(\phi, T_h, M, \boldsymbol{Y}\right) = \begin{bmatrix} dT_{c1} \\ dT_{c2} \\ dT_{c3} \\ dT_{c4} \\ dT_{e1} \\ dT_{e2} \\ dT_{e3} \\ dT_{e4} \end{bmatrix}, \quad \boldsymbol{Y}\left(\phi_0, T_{h0}, M_0\right) = \boldsymbol{Y}_0 \tag{2.29}$$

where the variables in bold represent vector quantities with dimensions 8x1. Thus, the numerical integration solution of (2.29) for the next time step is calculated using

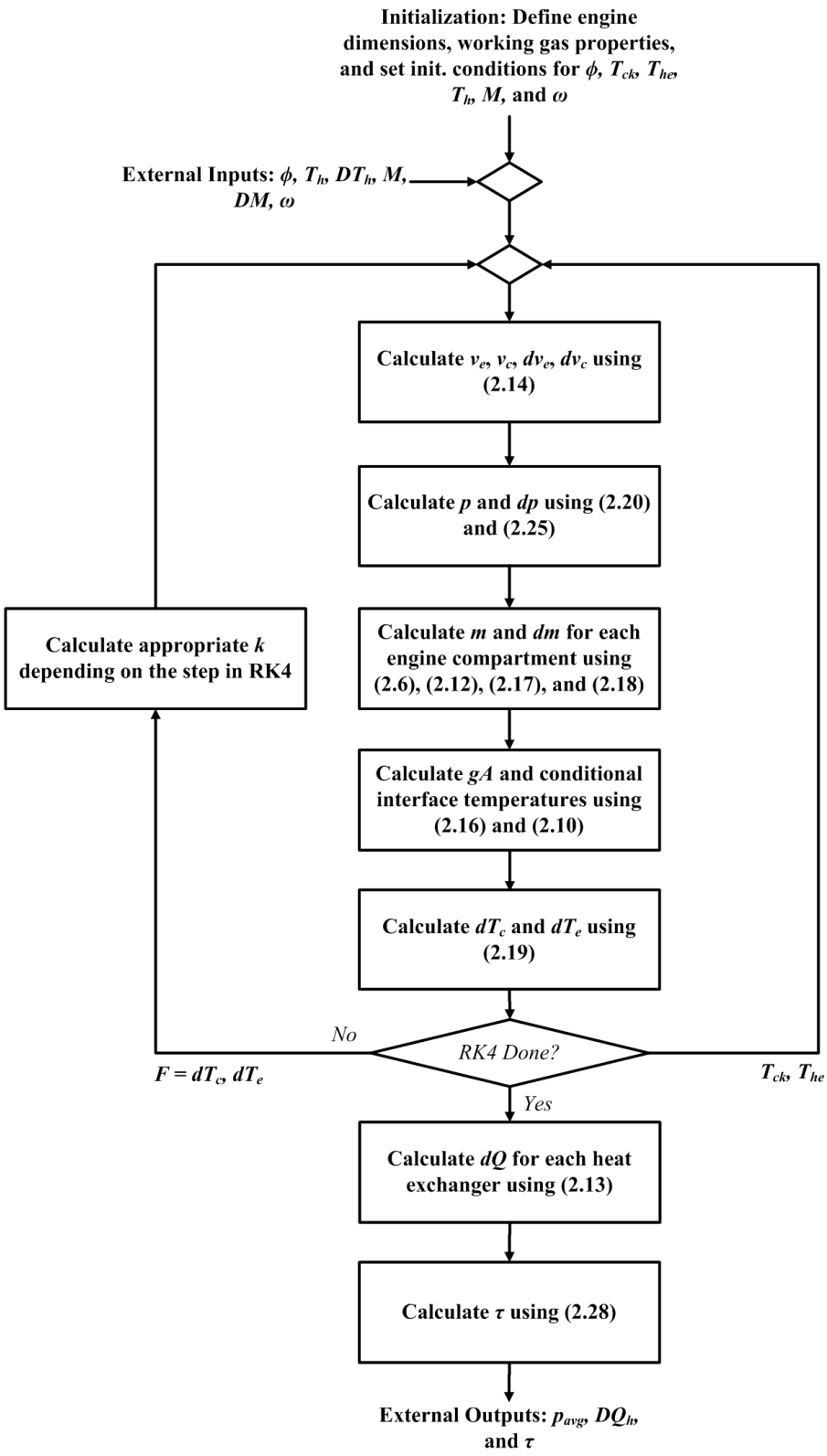

Figure 2.8: Stirling engine simulation flow diagram.

$$\begin{aligned} \boldsymbol{Y}_{n+1} &= \boldsymbol{Y}_n + \frac{1}{6}\left(\boldsymbol{k}_1 + 2\boldsymbol{k}_2 + 2\boldsymbol{k}_3 + \boldsymbol{k}_4\right) \\ \phi_{n+1} &= \phi_n + h \\ T_{h(n+1)} &= T_{h(n)} + hdT_h \\ M_{n+1} &= M_n + hdM \end{aligned} \tag{2.30}$$

where

$$\begin{aligned} \boldsymbol{k}_1 &= h\boldsymbol{F}\left(\phi_n, T_{h(n)}, M_n, \boldsymbol{Y}_n\right) \\ \boldsymbol{k}_2 &= h\boldsymbol{F}\left(\phi_n + 0.5h, T_{h(n)} + 0.5hdT_h, M_n + 0.5hdM, \boldsymbol{Y}_n + 0.5\boldsymbol{k}_1\right) \\ \boldsymbol{k}_3 &= h\boldsymbol{F}\left(\phi_n + 0.5h, T_{h(n)} + 0.5hdT_h, M_n + 0.5hdM, \boldsymbol{Y}_n + 0.5\boldsymbol{k}_2\right) \\ \boldsymbol{k}_4 &= h\boldsymbol{F}\left(\phi_n + h, T_{h(n)} + hdT_h, M_n + hdM, \boldsymbol{Y}_n + \boldsymbol{k}_3\right) \end{aligned} \tag{2.31}$$

and

$$h = \omega\Delta t \tag{2.32}$$

where Δt is the simulation time step. Calculating $\boldsymbol{k}_1$-$\boldsymbol{k}_4$ in (2.31) requires going through the pressure, mass, interface temperature and interface mass flow calculations individually for each $\boldsymbol{k}$, as shown by the flow diagram in Fig. 2.8, since dT_c and dT_e depend on all of these parameters. The integration loop shown in Fig. 2.8 is iterated 5 times for each simulation time step Δt: 4 times to calculate $\boldsymbol{k}_1$-$\boldsymbol{k}_4$, giving the final solution of $T_{c(1\text{-}4)}$ and $T_{e(1\text{-}4)}$, and once to calculate the final pressures, temperatures, and mass flows to be used in the torque τ and heat transfer DQ_h calculations. The final outputs of the Stirling engine simulation block are the average of the quadrant pressures, given by

$$p_{avg} = \frac{p_1 + p_2 + p_3 + p_4}{4} \tag{2.33}$$

the engine torque, calculated by (2.28), and the total heat absorbed by the Stirling engine, given by

$$DQ_h = \omega\left(dQ_{h1} + dQ_{h2} + dQ_{h3} + dQ_{h14}\right) \tag{2.34}$$

where converting a derivative with respect to the crank angle ϕ to a derivative with respect to time t is calculated by

$$Dz = \frac{dz}{dt} = \frac{d\phi}{dt}\frac{dz}{d\phi} = \omega\, dz \tag{2.35}$$

where z is an arbitrary variable that is a function of ϕ and t.

Combining the concentrator, receiver, Stirling engine, control systems, and induction generator models gives the diagram shown in Fig. 2.9. External inputs to the system include the solar irradiance I and heater/absorber temperature set point T_h*. The solar irradiance is an input to the concentrator/receiver block diagram shown in Fig. 2.1. The heater/absorber temperature set point T_h* is an input into the control system, which is discussed in more detail in the next chapter. The control system decides the quantity of working gas M to supply to the engine based on the heater/absorber temperature T_h, the engine pressure p_{avg}, and the engine/generator shaft speed ω. The induction generator, whose modeling methods are well documented and not discussed in this thesis, calculates the shaft speed, which serves as an input to the Stirling engine model discussed above. The torque generated by the engine model serves as an input to the induction generator model. The diagram of Fig. 2.9 is developed in PSCAD/EMTDC, using the built-in induction machine model as the generator. Custom FORTRAN code is written to model the Stirling engine and perform the numerical integration, as discussed above.

2.5 Conclusion

The models of the DS system components discussed in this chapter permit dynamic simulation of a grid-connected DS system. Such a model is valuable for understanding the behavior of a DS system under various transient conditions, including variations in solar irradiance and grid transients. However, the missing link in the DS system model is the control systems, which vary the amount of working gas in the Stirling engine. The performance of the control systems ultimately determine how a system operates in transient conditions, a topic which is discussed in detail in the next chapter.

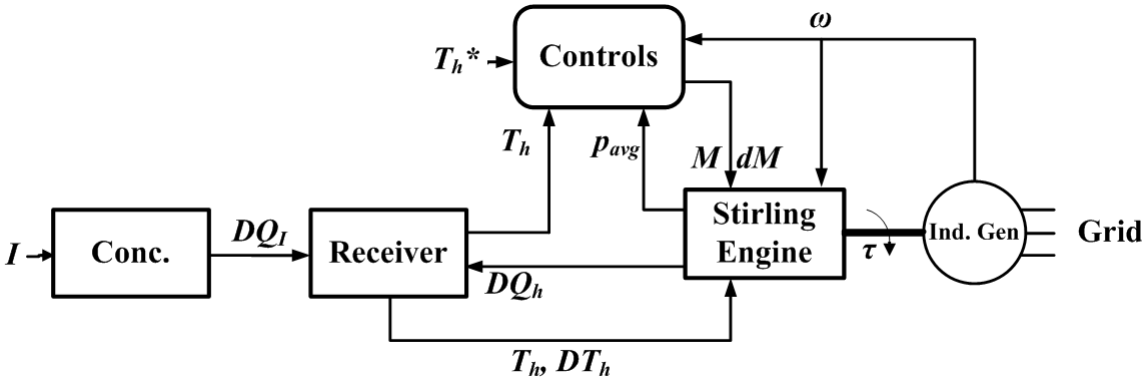

Figure 2.9: Dish-Stirling simulation block diagram.

CHAPTER 3

CONTROL SYSTEMS

3.1 Introduction

The primary control objective within the power conversion unit of a dish-Stirling (DS) system is to maintain the absorber temperature within a safe operating region. The temperature should be kept as high as possible to maximize the thermal efficiency of the Stirling engine, but should also not exceed the thermal rating of the absorber material. The temperature is controlled by varying the working gas pressure, achieved by adding or removing working gas to/from the engine. Changing the pressure of the Stirling engine working gas changes the quantity of mass flow through the absorber, thereby changing the amount of heat removed from the absorber. Since the input thermal energy from the sun is rather unpredictable and intermittent during daily operation, the pressure control must respond quickly enough to respond to changes in irradiance caused by cloud cover.

During normal operation, the Stirling engine shaft speed is not controlled but depends on the amount of available torque from the engine being balanced by the counter torque of the induction generator connected to the electric power network. However, in the event of a grid fault, the generator torque collapses and the shaft speed increases rapidly, potentially reaching speeds that could damage engine components or prevent the system from recovering from a grid fault. In such cases, the rapid increase in speed must be mitigated. The Stirling engine torque, therefore, has to be reduced rapidly in order to prevent the speed from increasing too much. Chapter 2 explained that the Stirling engine torque is a result of the working gas pressure acting on the pistons. Therefore, decreasing the working gas pressure has the effect of decreasing the engine's torque. During such a grid fault condition, the problem arises of whether to continue controlling the absorber temperature or to control the shaft speed, since the pressure control system cannot do

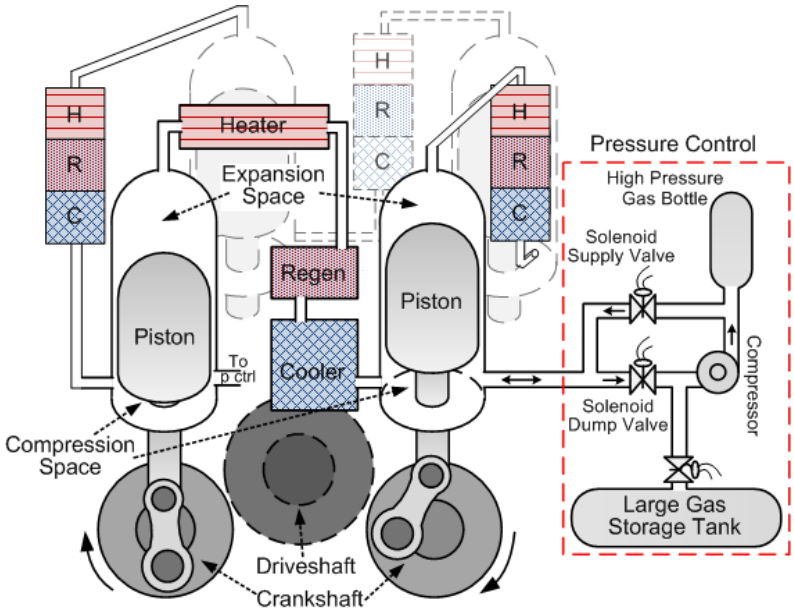

Figure 3.1: Pressure control system connection to Stirling engine.

both simultaneously. As discussed in more detail in the sections to follow, mitigating the shaft speed increase during a grid fault has the simultaneous effect of an uncontrolled rise in absorber temperature. However, it is assumed that the length of grid fault is short enough (hundreds of milliseconds) that the absorber material can withstand such a short duration increase in temperature. Such a tradeoff in design is assumed to be acceptable in order to gain the added protection of system components from damage that may be caused from over-speed and also enhance of the fault ride-through capability of the system. A more detailed analysis of fault ride-through capability is deferred until the next chapter.

3.2 Pressure Control System

A physical layout of the pressure control system (PCS) and interconnection with the Stirling engine is illustrated in Figure 3.1. The modeled PCS follows the systems described in [12], [23], [24], and [26]. The PCS consists of two working gas storage tanks; namely, the high pressure storage tank and the low pressure storage tank. Two control valves connect the high and low pressure storage tanks to the Stirling engine,

known as the *supply valve* and *dump valve*. If an increase in the engine working gas pressure is commanded, the supply valve opens and gas flows from the high pressure storage tank to the engine, increasing the total mass M (kg) of working gas inside the engine. Conversely, a decrease in the engine pressure results from opening the dump valve, and gas flows from the engine to the low pressure storage tank. The compressor pumps the working gas back to the high pressure storage tank from the low pressure tank, ensuring an adequate supply of high pressure working gas at all times. For the simulation and modeling in this thesis, it is assumed that an adequate amount of gas is always available for control purposes.

Solenoid valves are used for the supply and dump valves [23] [24], where modulation techniques can be used to regulate the flow of gas through the valve [25]. Since the Stirling engine is a closed system, the supply and dump valves are closed in steady state. Only when a change in operating point occurs does one of these valves open, such as the case when the irradiance increases, where the supply valve will open to increase the pressure. The solenoid valves are assumed to be pulse-width modulated (PWM) valves, where the valves are turned on and off successively, delivering mass in discrete packets [32]. The modulation frequencies of solenoid valves range from 20 Hz to 80 Hz, and the mass flow rate is proportional to the averaged spool position [32], where the "spool" is the magnetic piece of the solenoid valve that reacts to the voltage applied to the solenoid coils, and either opens or closes the valve. The solenoid valves are modeled as a first order system, given by

$$\frac{gA_{SV}(s)}{C(s)} = \frac{K_v}{1 + sT_v} \tag{3.1}$$

where gA_{SV} is the mass flow in the solenoid valve (kg/s), C is the commanded mass flow rate, s is the Laplace transform variable, and K_v and T_v are the gain and time constant of the valve, respectively. The pressure of the storage tanks are assumed to be constant, and, according to [19], the mass flow through the open valve can be approximated by

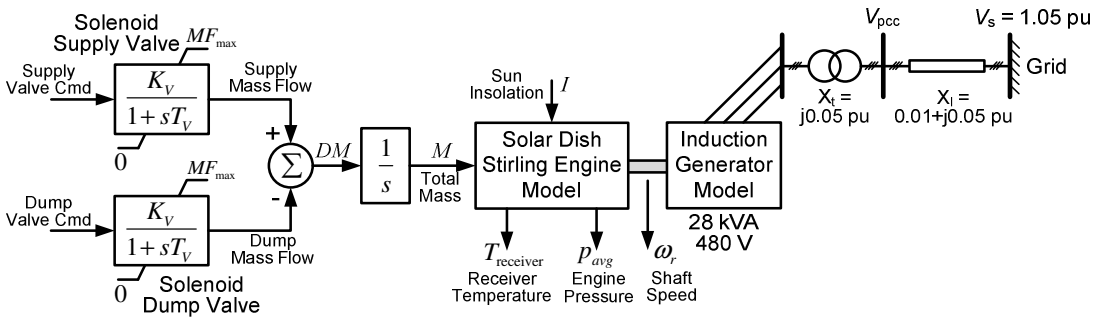

Figure 3.2: Block diagram of dish-Stirling system model with pressure control system supply and dump valves.

$$gA = \rho x \frac{\pi D_p^2}{4} \tag{3.2}$$

where ρ is the gas density (kg/m^3), D_p is the pipe diameter (m), and x is given by

$$x = \sqrt{\frac{2D_p\left(p_{st} - p\right)}{fL\rho}} \tag{3.3}$$

where p_{st} is the high pressure storage tank pressure (Pa), f is the friction factor, and L is the length of the pipe (m). Thus, assuming the minimum working gas pressure for p, the mass flow rate limit is a function of the pipe dimensions, and can be calculated using (3.2) and (3.3). The pressure of the high pressure gas storage tank and the pipe dimensions connecting the gas storage tank to the engine play a major part in the control system performance. These parameters affect the speed at which the PCS can respond during transients, particularly during grid faults.

A block diagram of the pressure control system is shown in Fig. 3.2. The total working gas mass M is calculated by integrating the mass flow rate output DM (kg/s) from the solenoid valve models. M and DM serve as inputs to the ideal adiabatic Stirling engine model discussed in the previous chapter. The supply and dump valve commands are supplied by the outputs of the block diagram shown in Fig. 3.3, where the pressure command is compared to the average pressure taken from the Stirling engine model discussed in the previous chapter, where the average pressure is given by

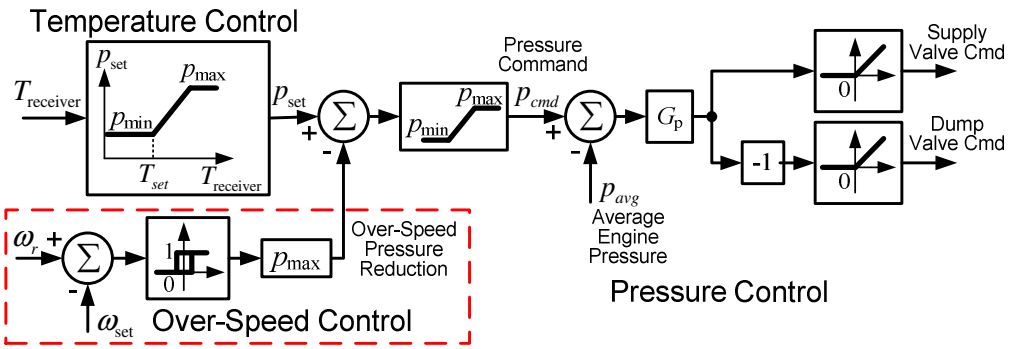

Figure 3.3: Temperature and over-speed control block diagram.

$$p_{avg} = \frac{p_1 + p_2 + p_3 + p_4}{4} \tag{3.4}$$

If the pressure difference is positive, the supply valve receives the control signal and mass flow command of the solenoid valve increases, thereby supplying more working gas to the Stirling engine from the high pressure storage tank. Conversely, a negative pressure difference will increase the mass flow command of the dump valve, returning working gas from the Stirling engine to the low pressure storage tank.

3.3 Temperature Control System

The heater temperature must be maintained as high as possible to maximize the efficiency of the Stirling engine, but must not be allowed to exceed the thermal rating of the receiver and heater/absorber materials. Regulation of the temperature is achieved by varying the working gas pressure. The temperature control system (TCS) generates a pressure control command based on the diagram shown in Fig. 3.4 [26]. The pressure remains at its minimum value until the heater temperature reaches the temperature set point, at which point the pressure command increases linearly with temperature increase. The pressure control system is only operable in the range of temperatures between T_{set} and (T_{set} + ΔT_{max}). In instances of unusually high solar irradiance, where the temperature exceeds (T_{set} + ΔT_{max}), and the pressure cannot increase further, other options for

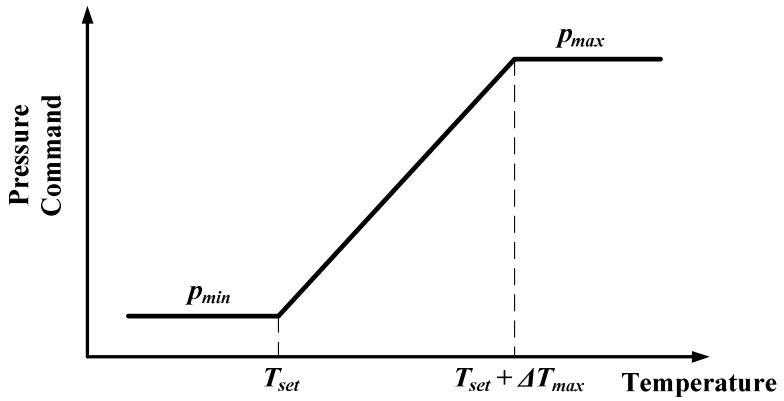

Figure 3.4: Pressure commanded by the temperature control system [26].

temperature regulation exist, such as supplementary cooling fans or a temporary de-tracking of the concentrator from the sun [8].

The temperature and pressure control systems of a DS unit operate in two different regions; namely, the controlled temperature region and the uncontrolled temperature region. In the uncontrolled temperature region, the irradiance is low and the heater temperature is below the temperature set point, and thus the pressure is maintained at its minimum value. The heater temperature thus varies with irradiance. At high irradiance levels, the pressure is varied to maintain the heater temperature within a narrow temperature range. The pressure control system kicks in at relatively low irradiance, thus the system is in the temperature control region during typical daily operation.

3.4 Over-Speed Control

In normal operating conditions, the Stirling engine/induction generator shaft speed is not controlled. Because of the torque characteristics of the engine, the speed is maintained over a narrow range of speed slightly higher than the synchronous grid frequency. In other words, at low irradiance, the engine produces just enough torque to keep the induction generator above synchronous speed, and at high irradiance, the engine does not produce enough torque to approach the unstable region of the induction

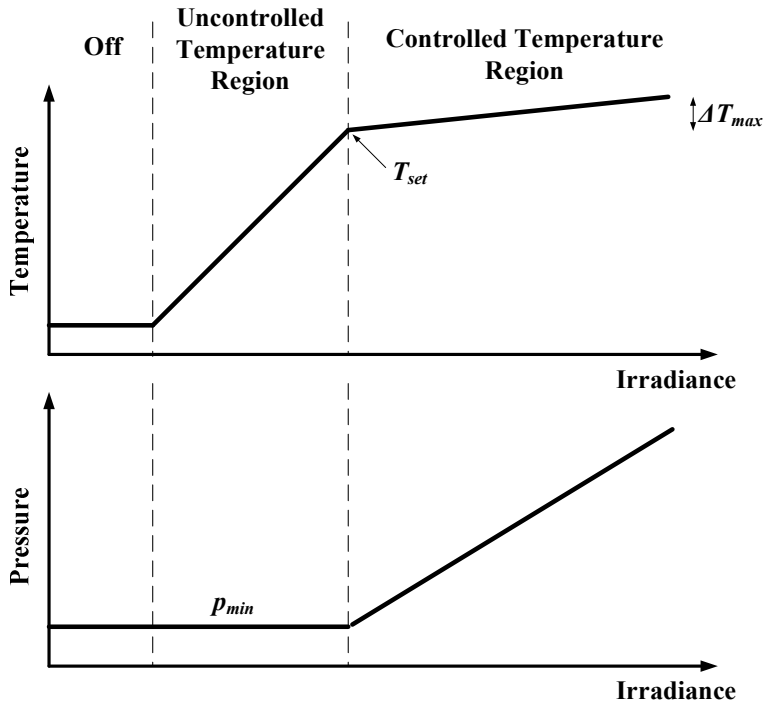

Figure 3.5: Controlled temperature region and uncontrolled temperature region.

machine, or the pull-out torque rating of the generator. However, in the event of a grid fault, the sudden loss of load torque causes a sharp increase in the shaft speed. Therefore, a mechanism for reducing the torque by the engine must be put in place to mitigate the sudden increase in speed. From (2.26), it is observed that the engine's torque can be reduced by decreasing the working gas pressure. The rapid decrease in pressure is achieved via a bypass valve [26], also known as a short-circuit valve [25], where working gas is quickly dumped out of the engine to decrease the pressure. For the present analysis, the dump valve shown in Fig. 3.1 is used to model this operation. The operation of the speed control system is illustrated in Fig. 3.3.

It is apparent that in the event of a grid fault, the temperature and speed control systems will try to counteract one another's operation. In other words, the rapid drop in pressure commanded by the speed control system will cause an increase in the heater temperature. This increase in temperature can be quite severe if the fault occurs during

high irradiance levels. In such a condition the TCS will respond by increasing the pressure set point. However, the pressure commanded by the TCS is limited to the maximum pressure set point. Therefore, when the shaft speed crosses the defined threshold ω_{set}, as shown in Fig. 3.3, the over-speed controller subtracts the pressure p_{max} from the TCS pressure set point, essentially disabling the TCS temporarily. A hysteresis controller is incorporated to prevent any problems with threshold recognition. Since grid faults are typically in the hundreds of millisecond time range, it is assumed that the increase in heater temperature for a short time range will have an insignificant impact on the receiver components.

3.5 Linearized Model

A linearized model of the Stirling engine pressure variations is developed to create a simplified method for tuning the pressure controller gain G_p shown in Fig. 3.3. The linearized model is developed assuming the system is operating in the controlled temperature region. In addition, the expansion and compression temperatures are assumed to be equal to the heater and cooler temperatures, respectively. The analysis is similar to the Stirling cycle analysis of Schmidt as discussed in [13]. The temperature profile of the various engine compartments in the linearized model appears in Fig. 3.6. Under the assumption that the control systems are in the controlled temperature region, the heater temperature stays within the narrow band ($T_{set} + \Delta T_{max}$). Therefore, for the linearized model, the heater temperature is assumed to remain constant at

$$T_h = T_{set} + \frac{\Delta T_{\max}}{2} \tag{3.5}$$

and the cooler temperature remains constant at ambient temperature.

The pressure of the engine working gas oscillates in steady state due to the sinusoidal volume variations of the expansion and compression spaces. The average working gas pressure between the four quadrant pressures is used in the control systems,

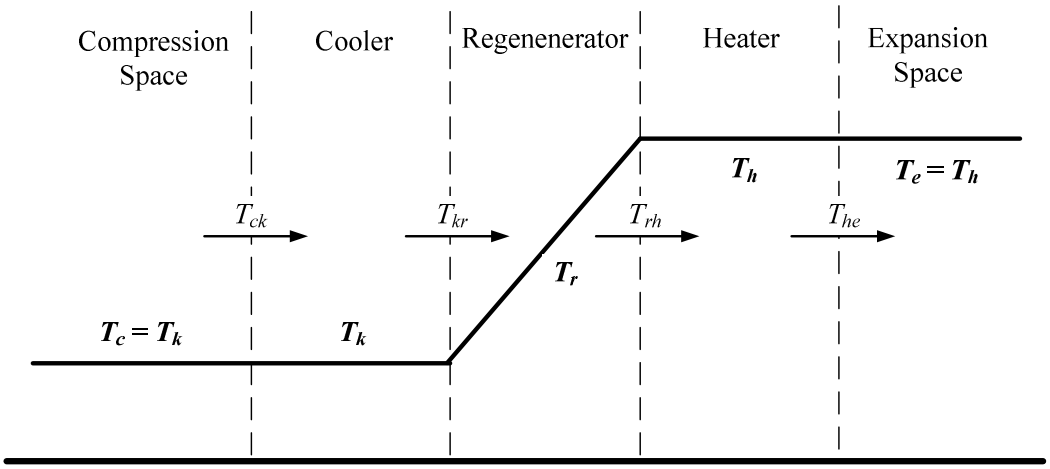

Figure 3.6: Simplified temperature distribution.

as calculated in (3.4). The four quadrant pressure oscillate around the same mean value at a phase shift of 90°, thus the average pressure has only minor oscillations in comparison to the individual quadrant pressures. Therefore, a linearized model is developed based upon an analytical expression for the mean pressure.

Using the engine diagram of Fig. 2.2 and the temperature distribution of Fig. 3.6, the pressure equation of (2.20) becomes

$$p = \frac{MR}{v_c / T_k + V_k / T_k + V_r / T_r + V_h / T_h + v_e / T_h} \tag{3.6}$$

Substituting the expressions for the expansion and compression space volumes of (2.14) and rearranging terms gives

$$p = \frac{MR}{\left[\frac{0.5V_s}{T_k T_h}\left[T_h \cos(\phi - \alpha) + T_k \cos(\phi)\right] + K\right]} \tag{3.7}$$

where K is given by

$$K = \frac{V_k}{T_k} + \frac{V_r}{T_r} + \frac{V_h}{T_h} + \frac{V_{dc} + 0.5V_s}{T_k} + \frac{V_{de} + 0.5V_s}{T_h} \tag{3.8}$$

Using trigonometric identities, (3.7) can be rewritten as

$$p = \frac{MR}{\left[\frac{0.5V_s}{T_k T_h}\left[(T_h \cos\alpha + T_k)\cos\phi + (T_h \sin\alpha)\sin\phi\right] + K\right]} \tag{3.9}$$

The linear combination of two trigonometric functions can be rewritten as

$$a\cos x + b\sin x = \sqrt{a^2 + b^2}\cos\left[x - \tan^{-1}\left(\frac{b}{a}\right)\right] \tag{3.10}$$

Applying (3.10) to (3.9) and rearranging terms gives the following expression for the pressure

$$p = \frac{A}{1 + B\cos(\phi - \theta)}M \tag{3.11}$$

where

$$A = \frac{R}{K}$$
$$B = \frac{V_s}{2T_h T_k K}\sqrt{(T_h \cos\alpha + T_k)^2 + (T_h \sin\alpha)^2} \tag{3.12}$$
$$\theta = \tan^{-1}\left(\frac{T_h \sin\alpha}{T_h \cos\alpha + T_k}\right)$$

The mean pressure is found using

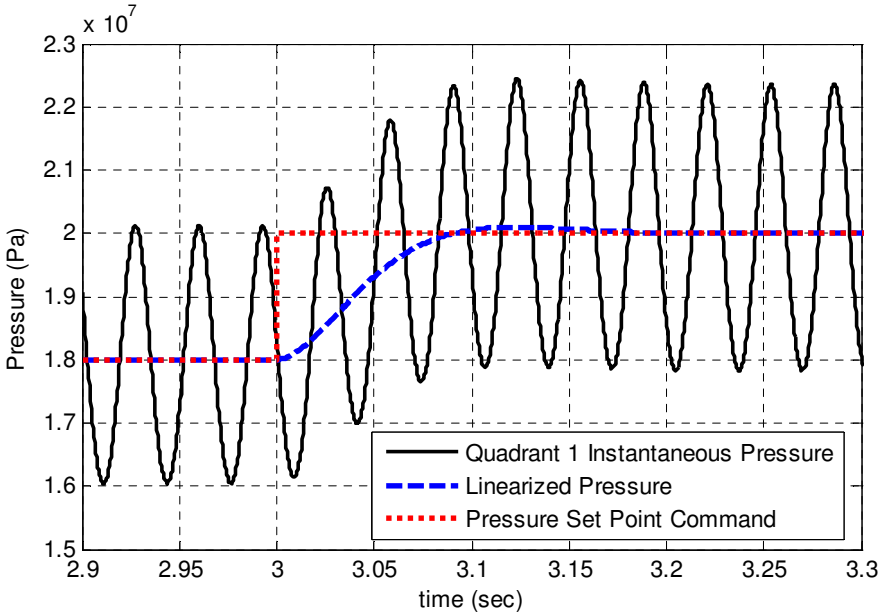

Figure 3.7: Comparison of the linear and non-linear pressure representations for a step change in pressure command.

$$p_{mean} = \frac{1}{2\pi}\int_0^{2\pi} p\,d\phi = \frac{1}{2\pi}\int_0^{2\pi} \frac{AM}{1+B\cos(\phi-\theta)}\,d\phi \tag{3.13}$$

Evaluation of this integral is rather lengthy and a solution is provided in [13], which requires use of the Cauchy residue theorem. The final solution is given by

$$p_{mean} = \frac{AM}{1-B}\sqrt{\frac{1-B}{1+B}} \tag{3.14}$$

Therefore the relationship between the quantity of working gas in the engine and the mean pressure is given by

$$\frac{p_{mean}}{M} = K_p = \frac{A}{1-B}\sqrt{\frac{1-B}{1+B}} \tag{3.15}$$

The constant K_p is derived assuming the engine is in steady state operation, and thus the total working gas mass M is assumed to be constant. Therefore the mean value of the pressure is calculated by integrating its defining equation over one revolution of the crankshaft. Therefore, the constant K_p defines the steady state pressure to be directly proportional to the total working gas mass. However, simulation results indicate that in transient operation, the time constants involved between a change in the total working gas mass and the pressure and torque are significantly smaller than the time constant of the solenoid valve. Thus, representing the pressure as proportional to the total working gas mass M in transient conditions produces little loss in accuracy. The plot of Fig. 3.7 compares the linearized pressure representation to the non-linear pressure of a single quadrant for a step change in the pressure commanded by the TCS. The linearized model simply removes the pressure oscillations, essentially acting as a low pass filter to the pressure variations.

3.6 Controller Tuning

The resulting linearized control loop of the PCS is shown in Fig. 3.8. The controller G_p of the dish-Stirling PCS must be tuned to give a desired system response.

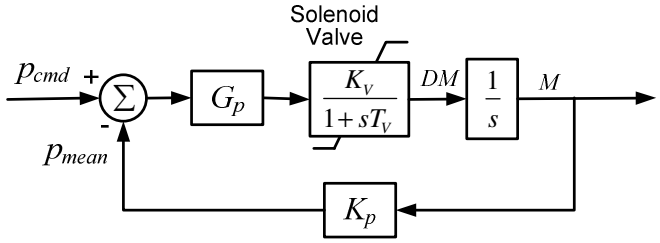

Figure 3.8: Linearized control loop of the pressure control system.

For the pressure control loop shown in Fig. 3.8, the open loop transfer function is given by

$$GH_o = \frac{G_p K_v}{s(1+sT_v)} \tag{3.16}$$

assuming that the control valve is in the linear (non-limiting) region. The closed loop transfer function is given by

$$GH_c = \frac{p_{mean}}{p_{cmd}} = \frac{K_p GH_o}{1+K_p GH_o} = \frac{G_p K_v K_p}{T_v s^2 + s + G_p K_v K_p} = \frac{G_p K_v K_p / T_v}{s^2 + (1/T_v)s + G_p K_v K_p / T_v} \tag{3.17}$$

The resulting closed loop transfer function of (3.17) is of the same form as the normalized second order system often used in linear control theory, with the general form given by

$$T(s) = \frac{\omega_n^2}{s^2 + 2\zeta\omega_n s + \omega_n^2} \tag{3.18}$$

where ξ is the damping ratio and ω_n is the natural frequency. Equating terms in (3.17) and (3.18), the damping ratio is given by

$$\xi = \frac{1}{2T_v\omega_n} = \frac{1}{2T_v\sqrt{G_p K_v K_p / T_v}} \tag{3.19}$$

The pressure controller gain G_p can thus be calculated by choosing a desired damping ratio, and solving for G_p in (3.19), given by

$$G_p = \frac{1}{4T_v\xi^2 K_v K_p} \tag{3.20}$$

The closed loop poles of (3.17) are in the left half plane for any value of G_p, therefore transient stability of the PCS is not an issue.

3.7 Conclusion

The control systems discussed in the present chapter are designed to maximize Stirling engine efficiency during normal operation by maintaining the heater/absorber temperature at the highest safe operating point. In addition, the control systems protect the system from over-speed of the generator shaft. The performance of the control systems must be tested under the transient conditions that a DS system is exposed to; cloud transients and electrical transients. The next chapter analyzes the simplest case of the DS system connected through a line and transformer to the grid, which is assumed to be an ideal voltage source. The next chapter also gives results and evaluates the performance of the control systems under grid faults. Simulation results of a DS system subject to cloud transient conditions are deferred until Chapter 5.

CHAPTER 4

SINGLE MACHINE INFINITE BUS ANALYSIS

4.1 Introduction

As dish-Stirling (DS) solar farms increase in capacity, grid interconnection issues become increasingly important, particularly regarding power factor correction and grid fault-ride-through capability [25]. Increasing penetration of DS solar farms within the utility grid requires simulation studies to assess the dish-Stirling system's impact on steady state and transient behavior of the grid, a topic which has received scant attention in the literature to date.

While there are presently no solar farm-specific grid interconnection requirements (GIR), it is reasonable to assume that the present requirements for wind farms [33] [34] will be similar if not identical to requirements of DS solar farms. The operating characteristics of wind farms and DS solar farms are quite similar. In particular, both technologies often make use of induction (asynchronous) generators which, individually, have relatively low power rating and are spread over a large geographic area. In addition, both technologies have an intermittent source of energy. Therefore, the technical challenges involved in ensuring that both wind and DS systems do not adversely affect power system operation and reliability are relatively similar. Many of the potential DS GIR are discussed in [25], while the next two chapters focus on the following requirements, that a solar farm should be capable of:

- Operating at a power factor anywhere in the range from 0.95 lagging to 0.95 leading at the point of common coupling (PCC) with the grid
- Maintaining a voltage at the PCC between 0.95 and 1.05 pu
- Riding through fault conditions, given by the voltage profile shown in Fig. 4.1

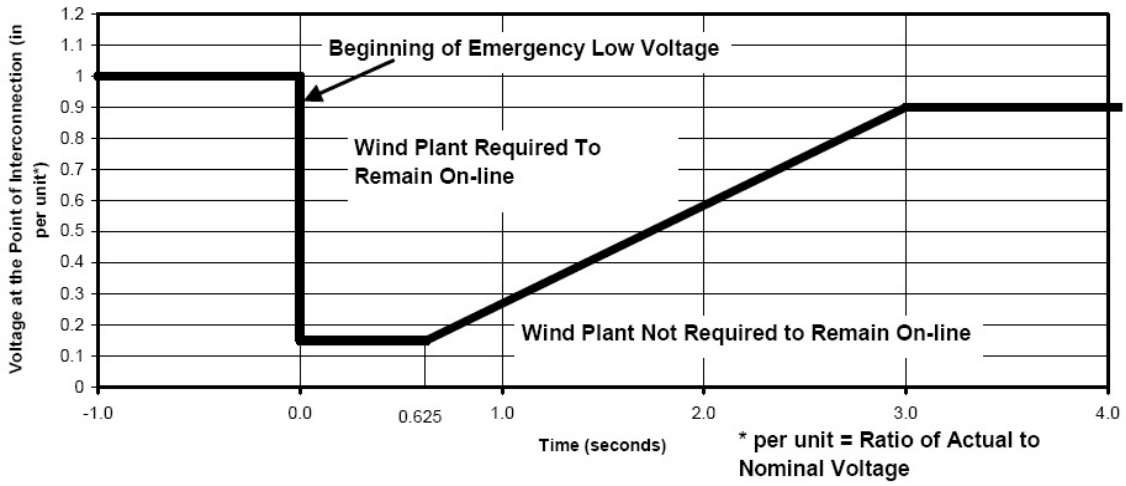

Figure 4.1: Low voltage ride-through requirements [33].

Meeting these requirements with DS solar farms requires additional infrastructure, since induction machines normally operate at a power factor outside of the range 0.95 lagging to 0.95 leading. In addition, induction machines absorb reactive power when operated as both a motor and a generator, which tends to reduce the voltage at the PCC. The amount of reactive power absorbed depends on the instantaneous solar irradiance, since the torque generated by the Stirling engine varies with input solar thermal energy. In addition, variations in solar irradiance, or cloud cover, cause variations in the voltage at the PCC, since the real power delivered and the reactive power absorbed by the solar farm fluctuates. Since there is no built-in means of voltage control with an induction machine, reactive power compensation is required to both increase the PCC voltage and mitigate the voltage variations due to cloud cover. Reactive power compensation is also required to bring the power factor within an acceptable range. The above requirements can be satisfied with various sources of reactive power compensation, including switched capacitors or static var compensators (SVCs).

In addition to power factor correction, wind farms are required to remain online during low voltage conditions induced by grid faults. The LVRT requirements are illustrated by the voltage profile shown in Fig. 4.1 [33], where the plant should be

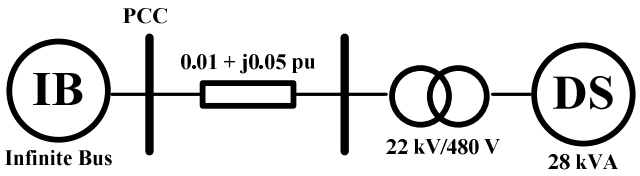

Figure 4.2: Connection of a single dish-Stirling (DS) unit in a single machine infinite bus model.

capable of remaining online for 0.15 pu voltage for up to 0.625 seconds, and should be capable of remaining online at a voltage of 0.9 pu indefinitely. Revised versions of LVRT requirements indicate the wind generator should be capable of remaining online for 0.15 seconds with 0 pu voltage [34]. Grid faults induce a sharp speed increase in the generator shaft, which can inhibit the machine's capability of riding through the fault once pre-fault voltage conditions are restored. Thus, additional controls are required to regulate the shaft speed during fault conditions. Dynamic reactive power compensation, such as SVCs and STATCOMs, can also aid in the LVRT of the DS system by supporting its terminal voltage.

4.2 Steady State Analysis

A one-line diagram of the system being considered is shown in Fig. 4.2. The single 28 kVA DS unit is connected to a step up transformer, and then through a transmission line to an infinite bus.

Before proceeding further, a notational clarification is established regarding

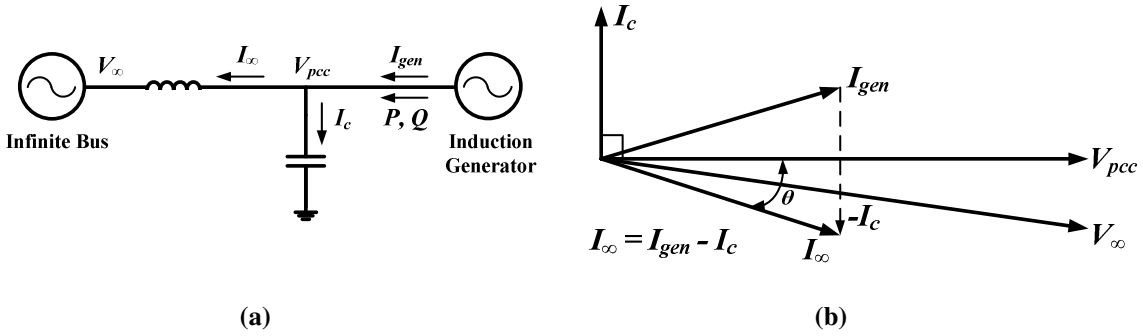

Figure 4.3: (a) Circuit diagram of induction generator connected to a network and (b) phasor diagram of labeled voltages and currents of (a).

power factor. The positive direction of the induction generator current, real power, and reactive power is specified as coming out of the generator terminals into the network, as shown by the simple circuit diagram shown in Fig. 4.3(a), where the infinite bus represents the network. The induction machine absorbs reactive power when operated as both a motor and a generator, therefore, using the defined sign convention, the reactive power supplied is negative. However, the power factor changes from lagging to leading when changing from motoring to generating operation, respectively. Without the capacitor bank shown in Fig. 4.3(a), the generator current I_{gen} is equal to the current I_{∞} entering the network, which is leading the voltage V_{pcc}, as shown by the phasor diagram in Fig. 4.3(b). Thus the induction generator is delivering power to the network with a leading power factor, similar to the operation of an under-excited synchronous generator. With the capacitor bank shown in Fig. 4.3(a) included, the current entering the network I_{∞} is the difference between the generator current and the capacitor bank current I_c.

The P-Q phasor diagram of Fig. 4.4 illustrates the amount of compensation required to meet power factor GIR for a single 25 kW dish-Stirling unit. Also shown in Fig. 4.4 is the power factor notation used for the four operating regions of the induction

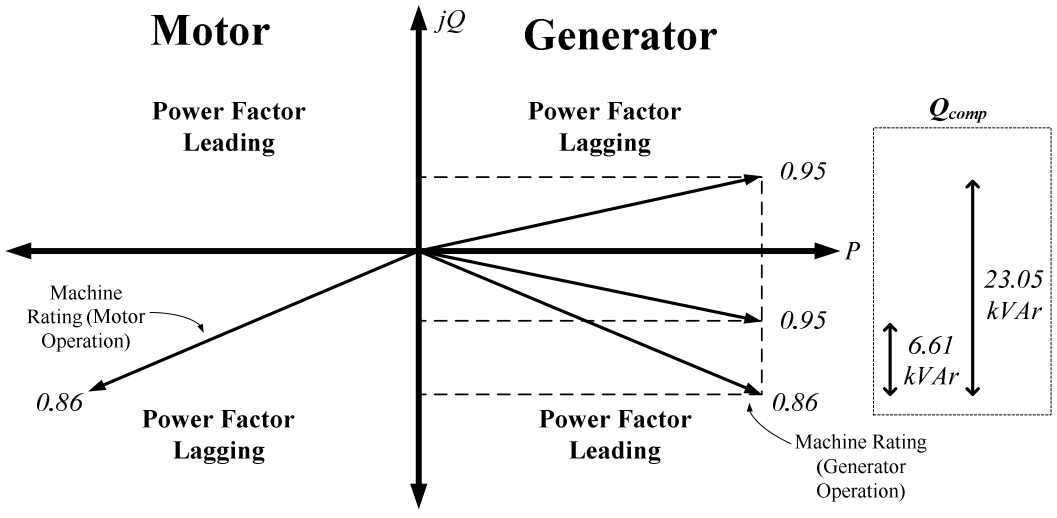

Figure 4.4: P-Q diagram of induction machine, showing amount of reactive power compensation required to meet grid interconnection requirements.

machine. Reactive power compensation requirements of DS solar farms can be calculated assuming rated voltage at the generator terminals, where the rated power factor of the induction machine is assumed. Thus, with a DS unit supplying rated power output of 25 kW and with a machine rated power factor of 0.86 leading, the reactive power absorbed, assuming no reactive power compensation, is given by

$$\begin{aligned} Q &= -|V||I|\sin\theta = -P\tan\theta \\ &= -\frac{25}{0.86}\sin\left(\cos^{-1}(0.86)\right) = -14.83 \ \ kVAr \end{aligned} \tag{4.1}$$

where θ is the angle between the current and voltage waveforms. The reactive power required to supply rated real power at a power factor from 0.95 leading to 0.95 lagging is calculated by

$$\begin{aligned} 0.95 \ \ leading \rightarrow Q_{comp} &= 14.83 - \frac{25}{0.95}\sin\left(\cos^{-1}(0.95)\right) \\ &= 6.61 \ \ kVAr \\ 0.95 \ \ lagging \rightarrow Q_{comp} &= 14.83 + \frac{25}{0.95}\sin\left(\cos^{-1}(0.95)\right) \\ &= 23.05 \ \ kVAr \end{aligned} \tag{4.2}$$

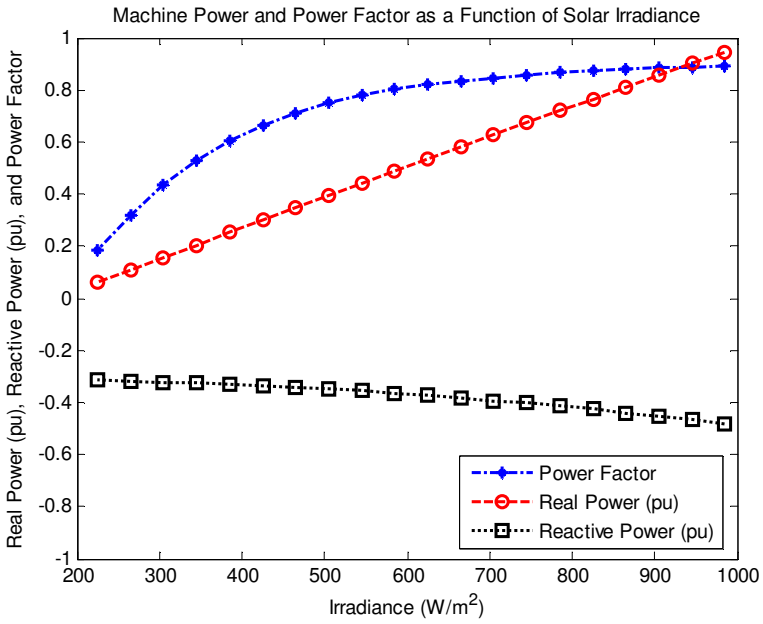

Figure 4.5: Steady state values of the dish-Stirling system real power, reactive power, and power factor as a function of solar irradiance.

Thus the variable reactive power compensation must have a capacity of at least 6.61 kVAr to meet the lower limit of the GIR.

Shown in Fig. 4.5 is the real power, reactive power, and power factor of the induction generator as a function of irradiance connected to an infinite bus as shown in Fig. 4.2. The range of irradiance is chosen to be between 200 and 1000 W/m^2 since this range is typical for most locations around the world, and the dish-Stirling system cannot generally operate at irradiance levels lower than 200 W/m^2 [12]. As expected, the real and reactive power magnitudes increase with irradiance and the power factor improves. The real and reactive power magnitudes decrease roughly linearly with irradiance, but the power factor decreases much more rapidly. Shown in Fig. 4.6 is the reactive power compensation required as a function of irradiance for meeting both the 0.95 leading requirement and 0.95 lagging requirement. The shaded region illustrates the range of compensation required to operate anywhere in the entire 0.95 leading to 0.95 lagging region. Therefore, since cloud cover will cause the irradiance to vary during the day, the reactive power compensation should at least be capable of operating along the lower line

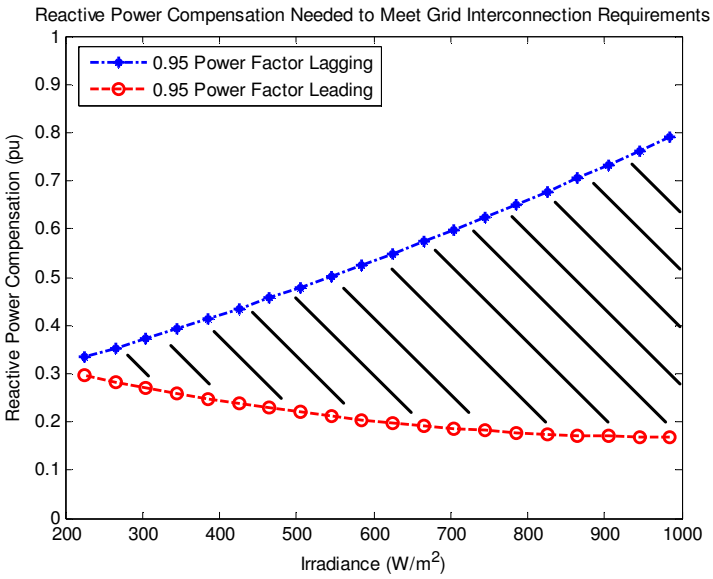

Figure 4.6: Reactive power compensation range to meet grid interconnection power factor requirements for varying solar irradiance.

of Fig. 4.6. For the case of switched capacitors, discrete quantities of reactive power compensation are available, thus choosing the proper values of capacitors allows for operation at discrete points within the shaded region shown in Fig. 4.6. Using continuously variable reactive power compensation, such as SVCs, the compensation can operate at any point within the shaded region if sized appropriately.

The torque speed curve of both the induction machine (electric torque) and the Stirling engine (mechanical torque) are shown in Fig. 4.7. Two curves are shown for the engine mechanical torque: one in which the irradiance is constant at 1000 W/m^2, and the other in which the irradiance is constant at 300 W/m^2. The intersection of the two engine torque curves with the electric machine's torque curve identifies the steady state speed at which the engine shaft rotates at the respective irradiance. At low irradiance, the induction machine operates at a lower speed (A_2 in Fig. 4.7), and vice versa. At high irradiance, there may be two possible steady-state operating points (A_1 and B_1 in Fig. 4.7). One corresponds to a stable operating point (A_1) and the other is unstable (B_1). The system is typically designed such that at different irradiance levels the steady-state

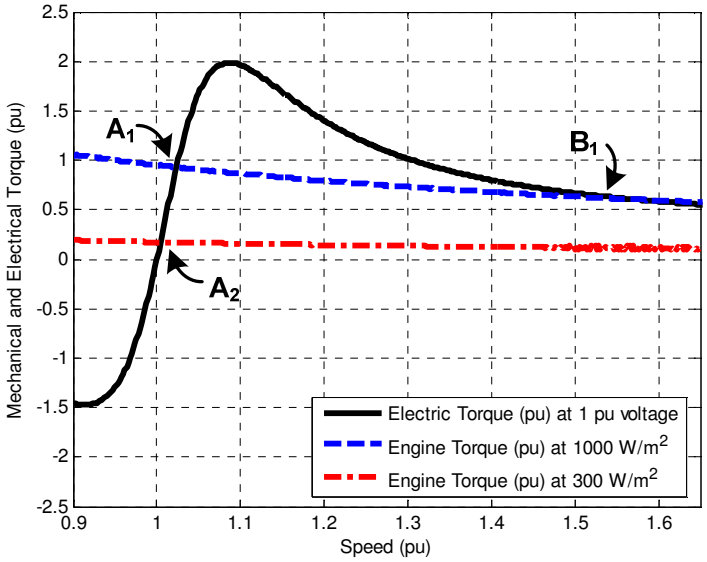

Figure 4.7: Induction machine electric torque and Stirling engine mechanical torque versus speed.

operating speed is relatively far away from the speed corresponding to the rated pull-out torque (2 pu in Fig. 4.7), ensuring stable steady-state operation. Under transient conditions, the system may become unstable once the operating speed exceeds the unstable operating point.

4.3 Transient Analysis

When a 150 msec three phase short circuit is applied somewhere along the transmission line of the diagram of Fig. 4.2, the Stirling engine/generator speed rapidly increases, causing the over-speed control to turn on as illustrated in Fig. 3.3. When the shaft speed exceeds ω_{set}, the dump valve opens to quickly remove working gas from the engine, having the effect of decreasing the pressure and thus the torque produced by the Stirling engine. Shown in Fig. 4.8(a) is a comparison of the pressure command and actual working gas pressure in the engine both with and without over-speed (OS) control. Without OS control, the pressure commanded is simply proportional to the heater temperature as shown in Fig. 4.8(b). Thus, since only minor changes in the heater temperature are induced by the increased speed of the generator shaft, the effects on pressure are minimal. However, when implementing OS control, the pressure command drops quickly shortly after the fault, and recovers shortly after the fault is cleared. Similarly, the engine and electric torques are compared for both the presence and absence of OS control, as shown in Fig. 4.8(c). When OS control is implemented, the engine torque starts to decrease shortly after the fault, attempting to mitigate the speed increase of the engine/generator shaft. Conversely, with no OS control, the torque changes very little since the pressure does not respond significantly to the speed increase. The speed increase during the fault, which is shown in Fig. 4.8(d), is reduced by nearly one-half when using over-speed control as opposed to no over-speed control. This significant reduction in the speed increase allows for faster recovery after the fault, in addition to increasing the probability of riding through the fault. The reactive power drawn by the

generator is also reduced when using OS control, as shown in Fig. 4.8(e). Because less reactive power is drawn by the generator after the fault, the voltage can recover faster as shown in Fig. 4.8(f).

One problem that arises in the use of OS control is the significant increase in heater temperature during the fault, as shown in Fig. 4.8(b). Because the OS control drops the pressure to its minimum value to decrease the torque, the heat absorbed by the Stirling engine from the receiver decreases. The concentrator is continuously tracking the sun, thus the thermal energy from the concentrated sunlight is temporarily stored in the receiver material, resulting in a temperature increase. It is unknown if this short-duration increase in temperature can damage the receiver material. If so, additional measures must be taken to cool the receiver. It is assumed that the capability of fault ride-through achieved by OS control outweighs the disadvantage of having a short term temperature increase.

4.4 Conclusion

While the SMIB model provides insight into the steady state and dynamic properties of a DS system, the network is highly idealistic. In practice, the voltage at the PCC between the DS system and the network will not remain at 1 pu, and limitations in the amount of current that can be drawn from the network during transient conditions affects system dynamic behavior. In addition, the DS system can adversely affect other generators within a network due to the added reactive power demand of the induction generator. Therefore, the next chapter includes an analysis of the steady state and transient behavior of a DS solar farm, but within a more realistic network that contains conventional generators, loads, and transmission lines. The modeled DS system is extended to a solar farm, which is a power plant consisting of thousands of individual DS units. The effects of varying irradiance and grid faults are analyzed and compared to the SMIB results given in the present chapter.

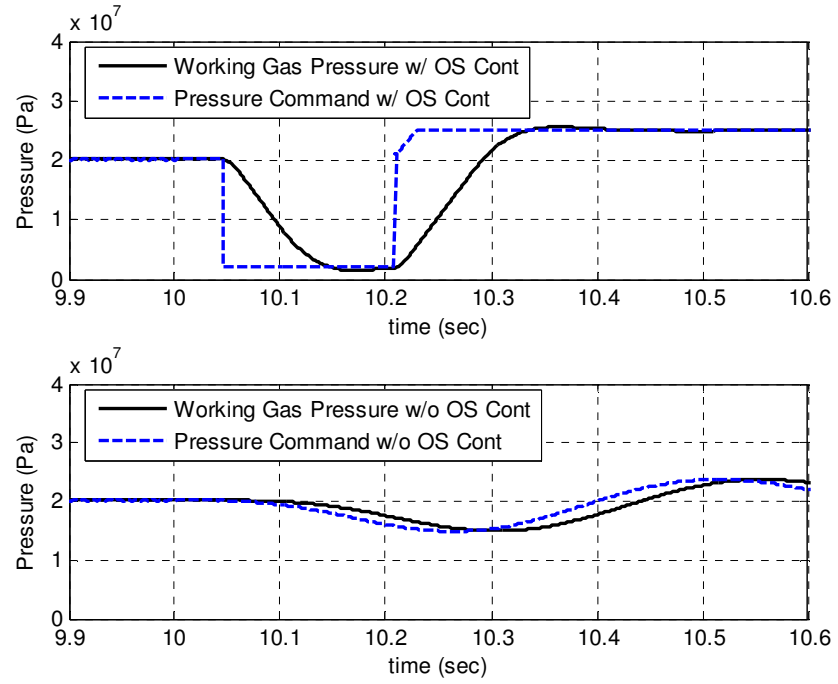

(a)

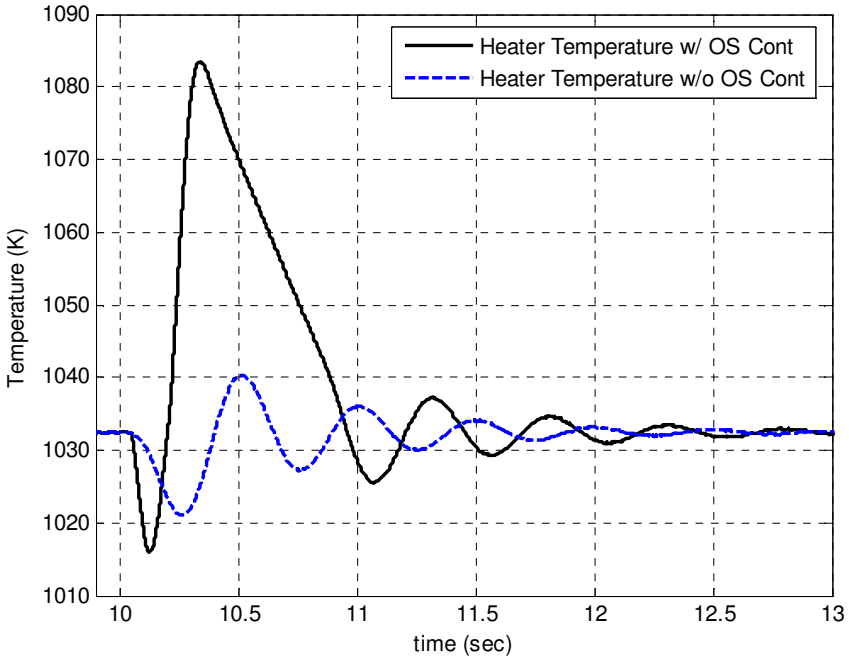

(b)

Figure 4.8: Simulation results for the (a) working gas pressure, (b) heater temperature, (c) mechanical and electrical torque, (d) generator shaft speed, (e) real and reactive power, and (f) generator voltage both with and without speed control for a 150 msec three phase to ground fault.

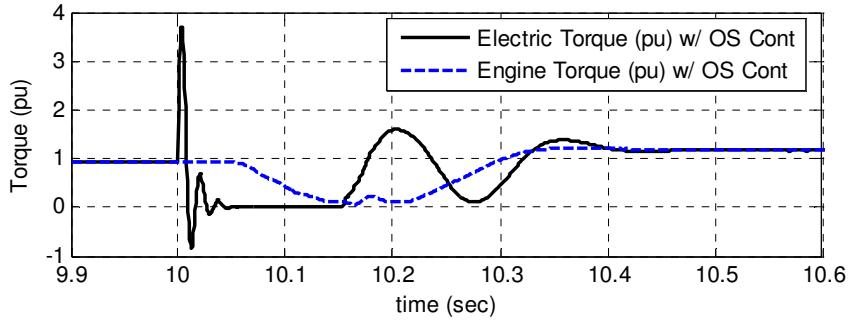

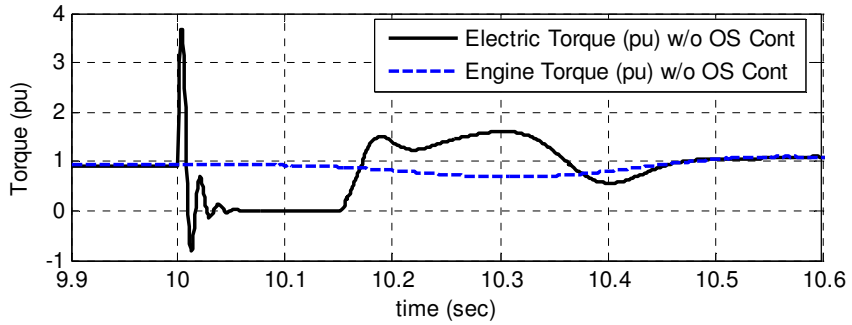

(c)

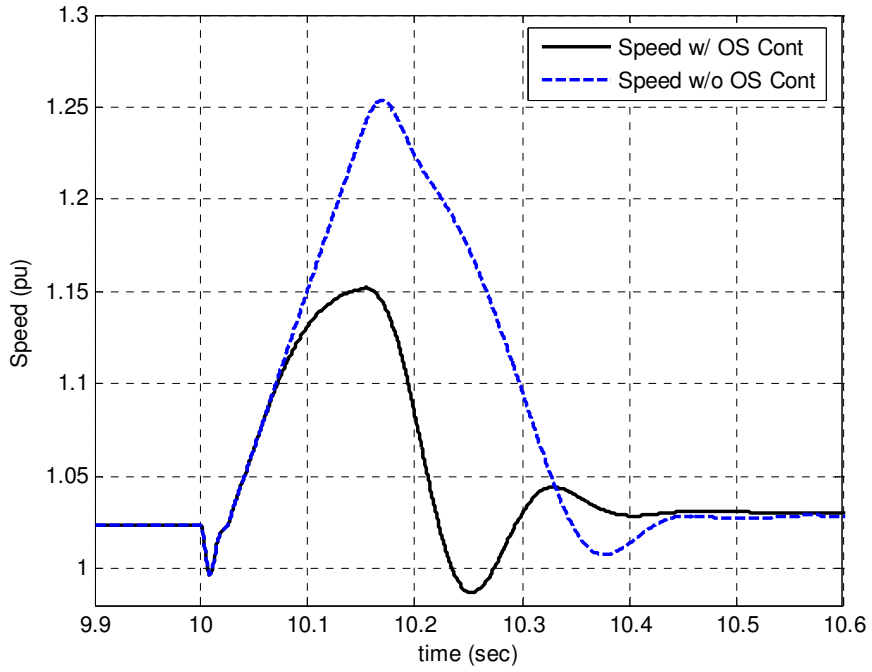

(d)

Figure 4.8 (cont'd): Simulation results for the (a) working gas pressure, (b) heater temperature, (c) mechanical and electrical torque, (d) generator shaft speed, (e) real and reactive power, and (f) generator voltage both with and without speed control for a 150 msec three phase to ground fault.

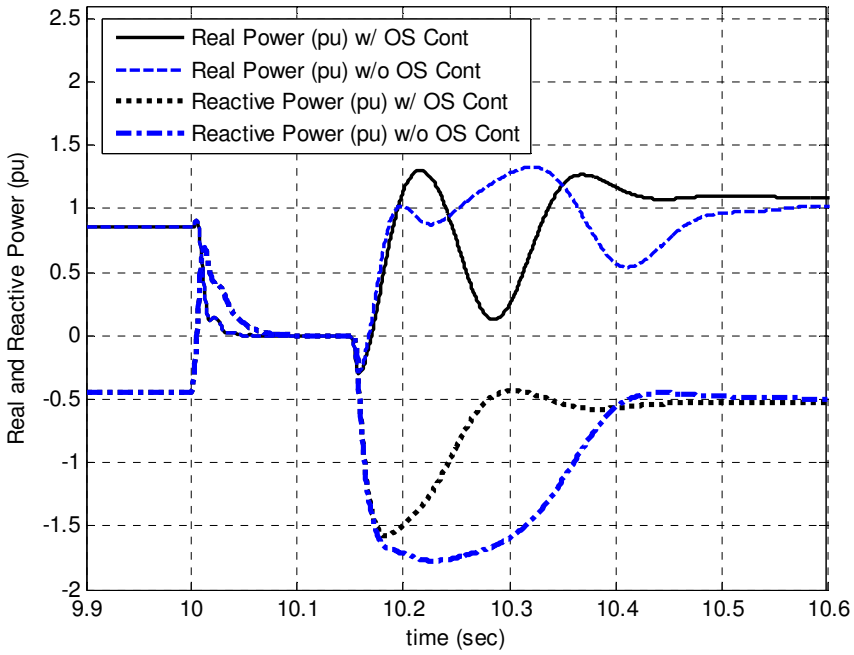

(e)

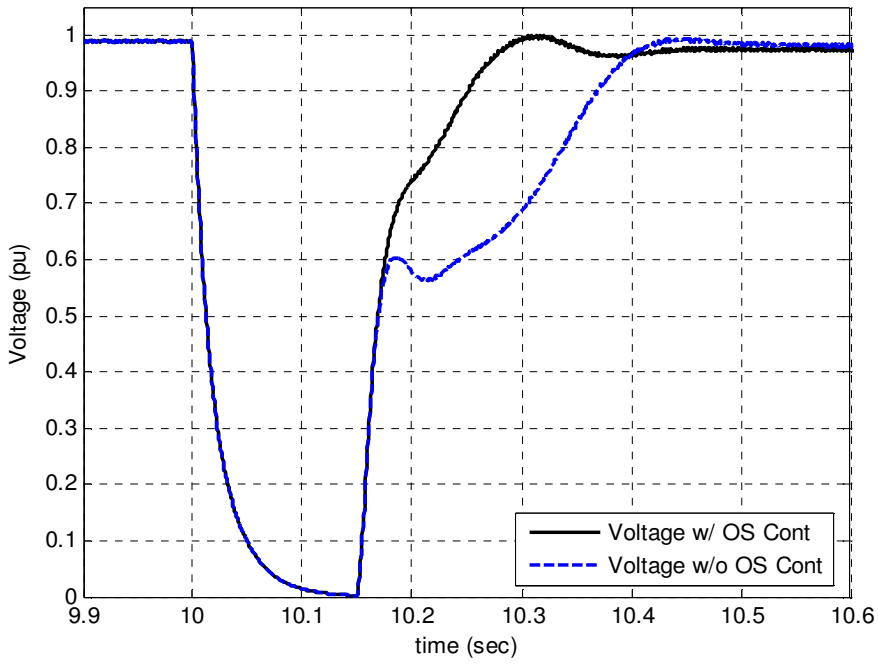

(f)

Figure 4.8 (cont'd): Simulation results for the (a) working gas pressure, (b) heater temperature, (c) mechanical and electrical torque, (d) generator shaft speed, (e) real and reactive power, and (f) generator voltage both with and without speed control for a 150 msec three phase to ground fault.

CHAPTER 5

SOLAR FARM IN 12-BUS NETWORK

5.1 Introduction

The 12-bus network used in the analysis and simulation of a dish-Stirling (DS) solar farm is shown in Fig. 5.1. The base-case network consists of 4 generators: three synchronous machines (G2, G3, & G4) and an infinite bus (G1). The various loads are modeled with passive components and the interconnecting lines are modeled using pi-equivalent models. The synchronous machines' excitation systems are included in the modeled network, along with the turbine governors and automatic voltage regulators (AVRs). More details of the 12-bus network are given in [35].

A solar farm consists of many individual DS units operating in parallel spread over a large geographic area. Solar farms can range in size from a few hundred DS units

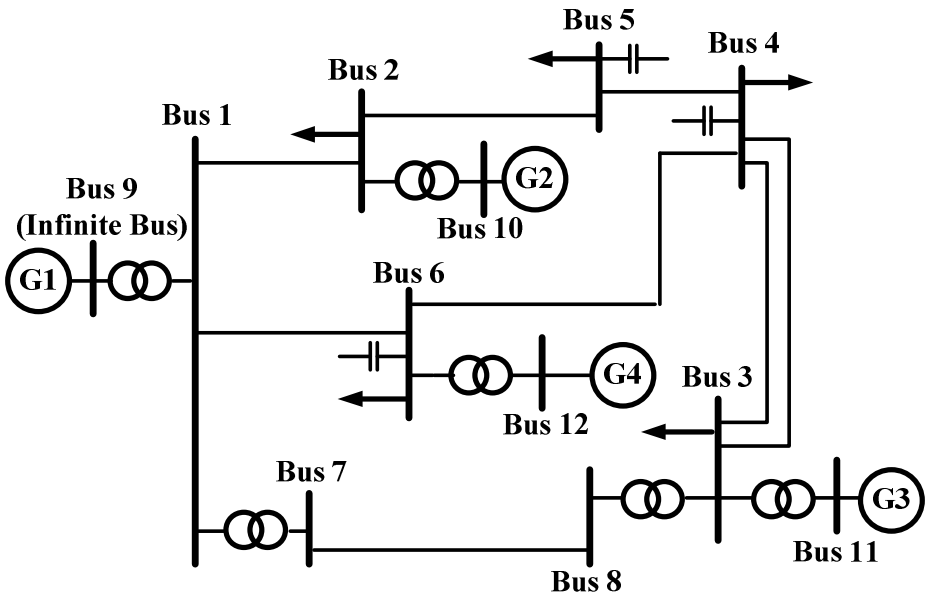

Figure 5.1: 12-Bus network used for analysis and simulation of the grid integration of a dish-Stirling solar farm.

to several thousand. As an example, the 1.5 MW plant currently installed in Peoria, AZ consists of 60 dish-Stirling units rated at 25 kW each. The plant contains four 25 kW units per acre of land, or 100 kW/acre [2]. A 500 MW solar farm would consist of 20,000 DS units spread out over approximately 5000 acres of land; simulation of such a plant becomes rather challenging since the irradiance levels can vary substantially over the entire land area of the solar farm. In addition, the computational effort required to simulate 20,000 induction generators and Stirling engines is not feasible. Therefore, reduced order models are required to make simulation of a large solar farm practical, yet still maintain a reasonable amount of accuracy.

This chapter describes a method to represent a large solar farm as a single equivalent generator, and evaluates the accuracy and limitations of this simplification. A solar farm is incorporated into the 12-bus network shown in Fig. 5.1 using the single machine equivalent solar farm model, and steady state and transient analysis provided. Different scenarios are discussed for connecting the solar farm into the 12-bus network, and the capability of meeting the grid interconnection requirements (GIR) regarding power factor correction and low voltage ride-through is evaluated.

5.2 Solar Farm Model Order Reduction

A detailed model of a 400 kW solar farm is shown in Fig. 5.2. The solar farm consists of 16 dish-Stirling units divided into 4 areas, each representing approximately one acre of land. The complete dynamics of each system is represented, including models of the concentrator, receiver, Stirling engine, and induction generator. The power network is simulated as an infinite bus and the line impedances and transformers between the generators and the infinite bus are included in the models. Each Stirling engine is represented by a set of 8 differential equations (given in Chapter 2), thus requiring substantial computational effort to simulate many DS units simultaneously. Thus, large solar farms have to be represented by simplified models.

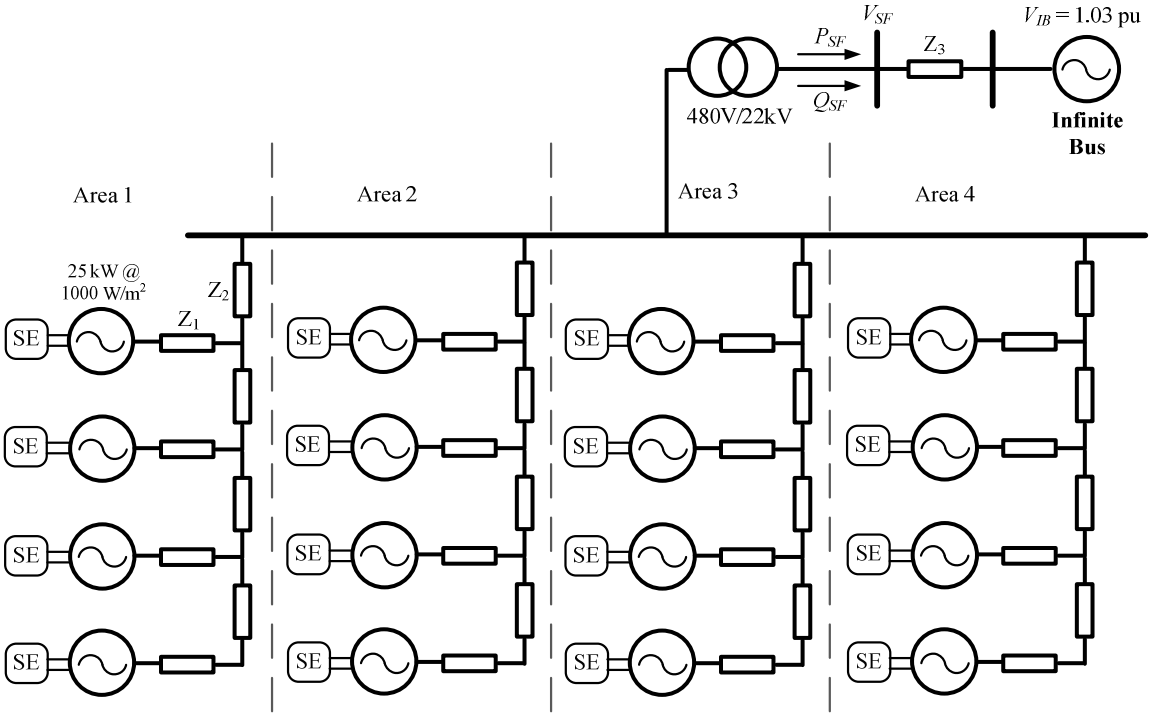

Figure 5.2: Model of a 400 kW dish-Stirling solar farm.

The results of Fig. 4.5 show that the real and reactive power of a DS unit are roughly linear functions of solar irradiance. Thus, the steady-state real power output of a dish-Stirling unit can be represented by an equation of the form

$$P = AI - B \tag{5.1}$$

where A and B represent the slope and intercept, respectively, of the real power line shown in Fig. 4.5, and I represents the solar irradiance. A similar relationship can be derived for the reactive power. Similarly, the power output of n dish-Stirling units operating in parallel, assuming identical impedances connecting them to a common voltage, is given by

$$\sum_{1}^{n} P_n = A\sum_{1}^{n} I_n - nB \tag{5.2}$$

where I_n and P_n represent the input irradiance and power output of the n^{th} DS unit. Thus the total power output of n DS units operating in parallel is a linear function of the sum-

total of the irradiance on all of the individual units. The n DS units can be represented as one machine in the per-unit system by

$$\frac{\sum_{1}^{n} P_n}{nP_{base}} = \frac{A\sum_{1}^{n} I_n}{nP_{base}} - \frac{nB}{nP_{base}} \tag{5.3}$$

where P_{base} is the base power of an individual DS unit, and nP_{base} is the base power of the equivalently rated machine representing the n individual machines. Thus, (5.3) can be written as

$$P_{pu} = \frac{A}{P_{base}}\left(\frac{1}{n}\sum_{1}^{n} I_n\right) - B_{pu} \tag{5.4}$$

Therefore the power output of a solar farm can be represented as a linear function of the average solar irradiance on the individual DS units, where the average irradiance over a solar farm of n DS units is defined by

$$I_{avg} = \frac{1}{n}\sum_{1}^{n} I_n \tag{5.5}$$

Using the average irradiance, the steady state power output of a solar farm can be represented by one equivalently rated machine using the average irradiance defined in (5.5). Thus, neglecting the line impedances connecting the individual dish-Stirling units to the step-up transformer, allows the diagram of the 400 kW solar farm shown in Fig. 5.2 to be simplified to the single machine (SM) model shown in Fig. 5.3. If the torque supplied by the Stirling engine is also defined in the per-unit system, then the same model of the Stirling engine used in the multi-machine (MM) can be applied to the SM model.

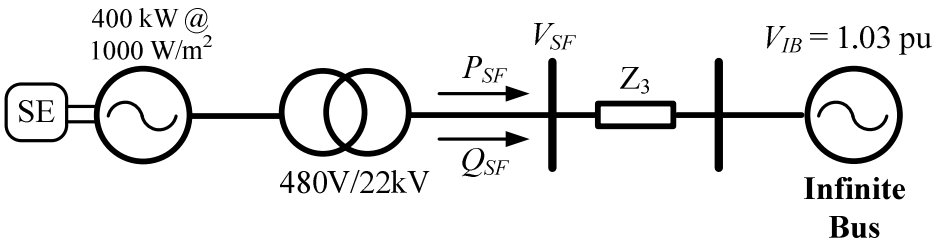

Figure 5.3: Simplified single machine model of 400 kW solar farm.

Simulation results comparing the real and reactive power output of the simplified SM solar farm model to the complete, MM model for varying irradiance is shown in Fig. 5.5 for the input irradiance waveforms shown in Fig. 5.4. Each area in Fig. 5.2 receives a different irradiance over the given time frame. As shown in Fig. 5.4, the irradiance levels of areas 1 and 3 are kept constant at 1000 W/m^2 and 300 W/m^2, respectively. Areas 2 and 4, on the other hand, receive an input irradiance representing a cloud transient, where an identical irradiance level strikes both areas, but area 2 receives the irradiance at a 90 second time delay from area 4. The simplified single-machine model receives the average irradiance shown in Fig. 5.4, which is calculated using the four area irradiances applied to (5.5). The variable input irradiance waveform is derived from irradiance data provided by NREL for Las Vegas, NV in one minute intervals [36]. This particular data is taken from several minutes during the month of August, and intentionally chosen because of the large changes in irradiance in a relatively short period of time, as would be typical of a cloud transient. In order to form a continuous irradiance waveform from the discrete data provided, a fifth-order polynomial approximation of the data points is

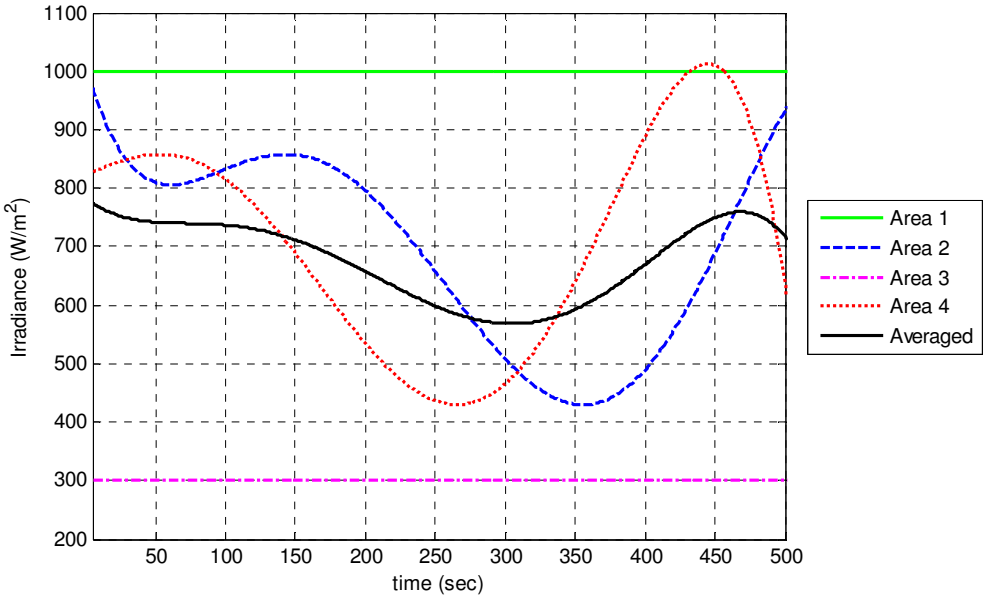

Figure 5.4: Input irradiance for the four solar farm areas and the averaged irradiance input for the single-machine model.

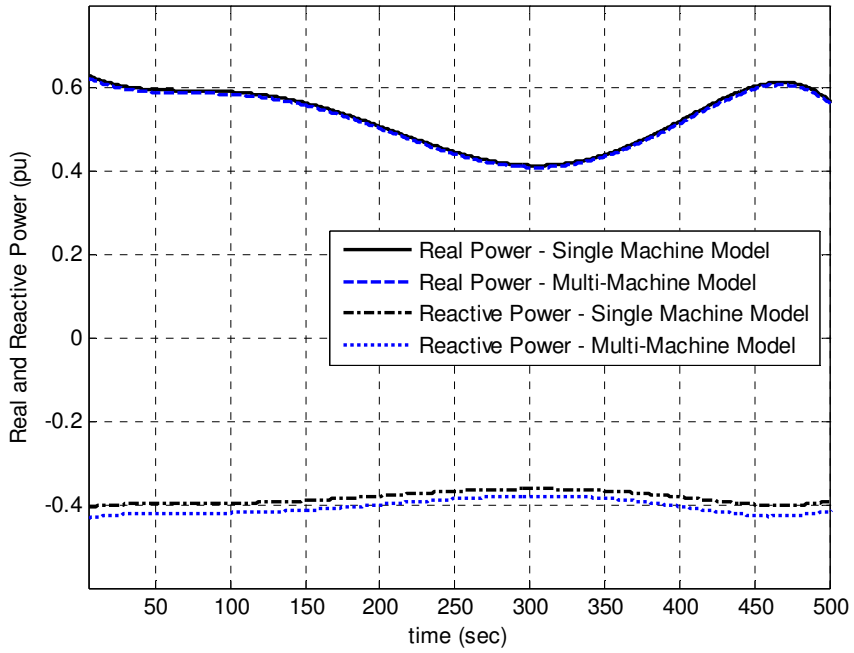

Figure 5.5: Real and reactive power output of the MM model and the SM model for the input irradiances shown in Fig. 5.4.

obtained from Microsoft Excel's built-in curve-fitting function.

The power output shown in Fig. 5.5 of the simplified SM model and the complete MM model displays a close correlation between the two models. Since the SM model neglects the line impedances connecting the DS system to the step-up transformer, the SM model gives a real power output slightly higher than the MM model and the amount of reactive power absorbed is slightly less in the SM model. The difference is greater between the reactive power waveforms than the real power waveforms since, in the neglected impedances of the MM model, the line reactances are significantly larger than the line resistances. The results shown in Fig. 5.5 indicate that, although the relationship between power output and irradiance derived in (5.1)-(5.4) assumes steady state operation, changes in irradiance are slow enough such that machine dynamics can be neglected with little loss in accuracy. Therefore, using the average irradiance input into an equivalently rated DS system yields accurate results for cloud transient simulations.

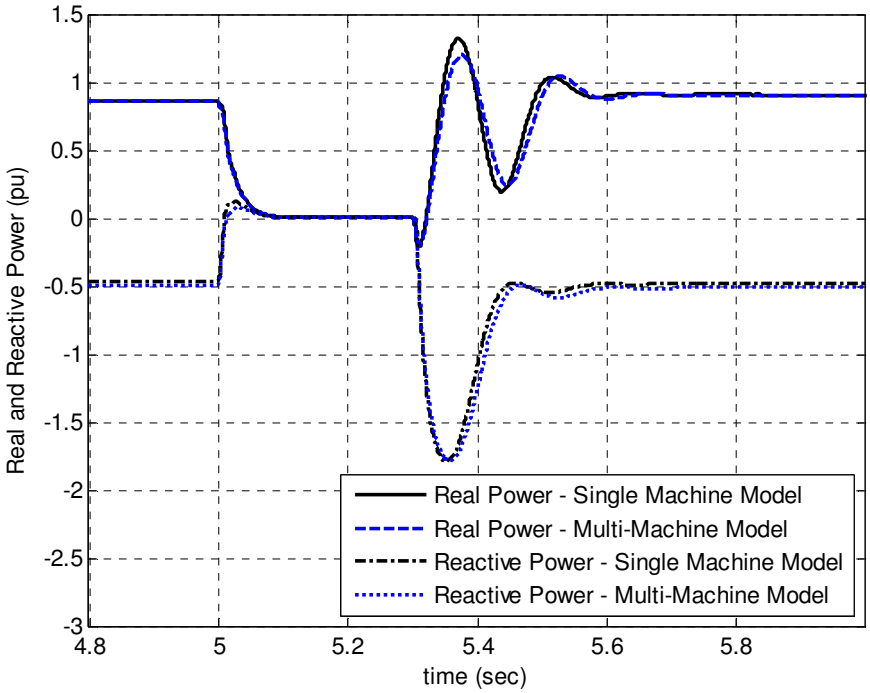

Figure 5.6: Real and reactive power output of the SM model and the MM model for a three phase to ground fault with uniform irradiance over the solar farm.

Simulation results for the real and reactive power output of the SM model and the MM model for a 300 msec three phase to ground fault are shown in Fig. 5.6. The fault occurs along the transmission lines shown in Figs. 5.2 and 5.3. The irradiance is assumed to remain constant during the fault, and is uniform in all 4 areas at 1000 W/m^2. Thus, prior to the fault, all 16 dish-Stirling units in the MM model are at the same torque and speed operating points. The results shown in Fig. 5.6 indicate that the SM model represents the MM model real and reactive power behavior quite accurately. Thus, with uniform irradiance over the solar farm, the SM model is a good approximation to the MM model transient behavior.

Simulation results for the real and reactive power output of the SM and MM models are shown in Fig. 5.7 for the same three phase to ground fault discussed in the previous paragraph, but with different irradiance levels on each area. Areas 1, 2, 3, and 4 receive constant irradiances of 1000, 300, 500, and 800 W/m^2 during the fault,

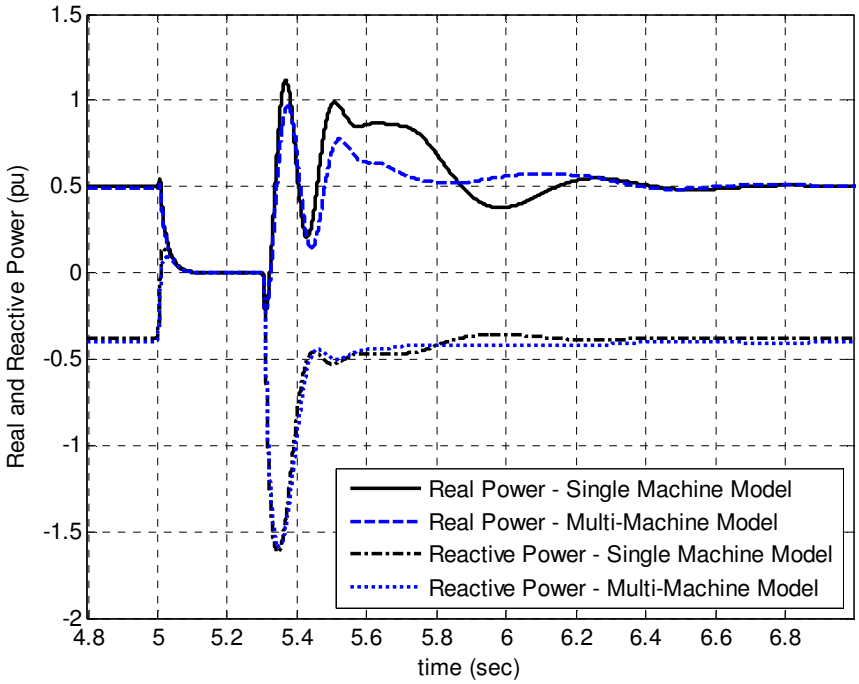

Figure 5.7: Real and reactive power output of the MM model and the SM model for a three phase to ground fault under different irradiance over the our areas.

respectively. In this case, the DS units in different areas are at different speed and torque operating points prior to the fault. Since the torque generated by the Stirling engines is different in each area, those units operating at higher irradiance experience a larger speed increase in the generator during the fault than those units at low-irradiance levels. Thus, as shown in Fig. 5.7, the real and reactive power of the SM model during the post-fault recovery deviate from the MM model, particularly the real power, due to the speed differences in the individual DS units in the MM model. While the SM model is less accurate under widely varying irradiance over the solar farm area than under uniform irradiance, the transient effects do not differ significantly enough such that using the SM equivalent model becomes unrealistic to use for transient studies.

The SM model of a DS solar farm significantly reduces the complexity and computational requirements of simulating the solar farm steady state and transient behavior. The general behavior of the SM model represents the MM model quite closely,

and the loss in accuracy in the SM model is a compromise that can be justified by the significant reduction in model and simulation complexity. Therefore, the SM model is used throughout the remainder of the chapter to represent large DS solar farms. Analysis of a solar farm within the larger, more realistic 12-bus network provides additional insights into the behavior of a solar farm under steady state and transient conditions.

5.3 12-Bus Network Steady-State Analysis

Several case studies are carried out in order to illustrate the impact of connecting a solar farm to a 12-bus power network, using different means of reactive power compensation in each case study.

5.3.1 Base Case

In the base case, generator 3 (G3) in the 12-bus network shown in Fig. 5.1 is a conventional thermal power plant, with a synchronous machine generating 200 MW. The AVR of G3 controls the voltage at bus 11 to 1.01 pu. Simulations indicate that G3 operates in the overexcited mode at a power factor of 0.75 lagging in steady state while maintaining the voltage at bus 11 at 1.01 pu. Operation at such a poor power factor is impractical, and is not typically done in practice. In addition, G3 is not meeting the grid interconnection requirement discussed in the previous chapter regarding power factor. The reason for the poor power factor is the load connected at bus 3, which is rated for 320 MW + j240 MVAr, which exceeds the rating of G3. Therefore, significant current must be drawn from connecting lines to supply this load, which requires the AVR of G3 to command the reactive power to make up for the voltage drop across connecting lines. In order to bring the power factor of G3 to unity, a capacitor bank can be inserted at bus 3 with a MVAr rating determined by

$$Q = P\tan\theta = 200\tan\left(\cos^{-1}(0.75)\right) = 176 \;\; MVAr \tag{5.1}$$

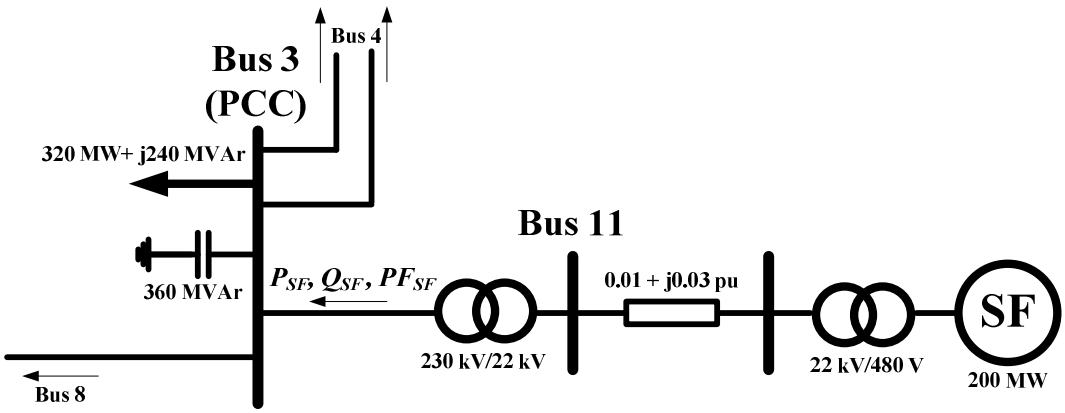

Figure 5.8: Connection diagram using only fixed compensation for voltage support in the integration of the solar farm at bus 11.

Simulation results indicate that with the capacitor bank of 176 MVAr in place, the synchronous machine's power factor is approximately unity in steady state, and the voltage at bus 11 is constant at 1.01 pu.

5.3.2 Solar Farm Connected to 12-Bus Network

5.3.2.1 No Reactive Power Compensation

Before incorporating the solar farm into the 12-bus network, the thermal generator (G3) is removed for the purpose of this case study. With no source connected to bus 11 or reactive power support at bus 3, the voltage at bus 3 drops to 0.78 pu. Adding a 200 MW rated solar farm (which consists of 8,000 25 kW dish-Stirling units operating at an irradiance level of 1000 W/m^2) to bus 11 reduces the voltage at bus 3 even further. However, the voltage at the PCC for a possible solar farm location would not realistically be at 0.78 pu, but adding a capacitor bank rated at 360 MVAr at bus 3 increases the bus 3 voltage to 1 pu (with no solar farm or G3 connected).

5.3.2.2 Fixed Compensation

In this case study, the 360 MVAr compensation at bus 3 is held fixed, and no other variable source of reactive power compensation is included. Simulation results for the voltage at the PCC as a function of irradiance level appears in Fig. 5.9. At high irradiance levels, the solar farm produces near rated power to the local load at bus 3, and less current is therefore drawn from other network busses. Since less current is drawn, the voltage drops across the connecting lines are less, and thus the 360 MVAr capacitor bank supplies more reactive power than needed, causing the voltage to rise to approximately 1.05 pu. However, at low irradiance levels, the power factor of the solar farm PF_{SF} follows that shown in Fig. 4.5, causing the voltage at the PCC (V_3) to drop since more current must be drawn from other busses to supply the load, in addition to the reactive power load of the solar farm.

The results of Fig. 5.9 illustrate the necessity of having variable reactive power compensation since the voltage V_3 changes with irradiance. Further, in more realistic systems, the loads will also vary throughout the day, which likely makes fixed

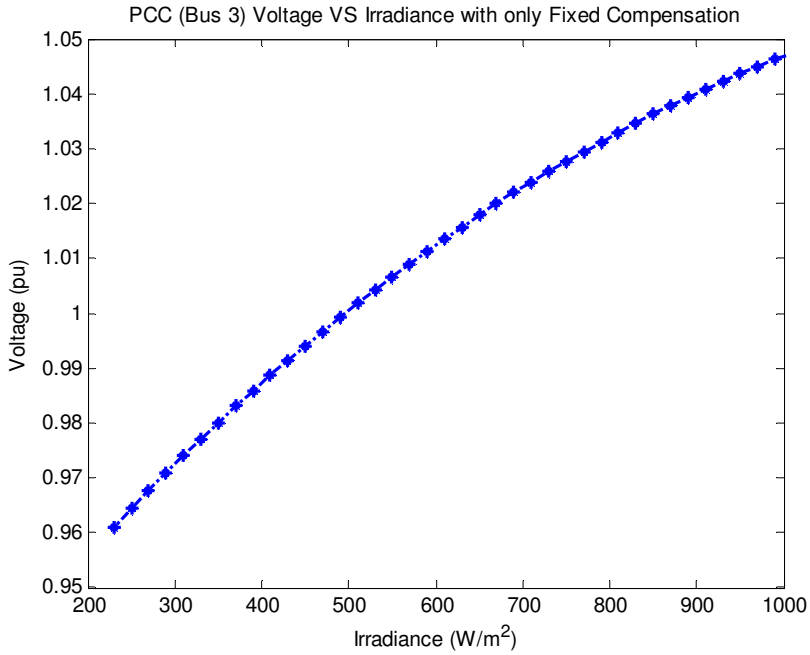

Figure 5.9: Bus 3 voltage versus solar irradiance with only fixed compensation.

compensation inadequate for maintaining the PCC voltage V_3 between 0.95 and 1.05 pu.

5.3.2.3 Variable Compensation

In this case study, the solar farm is again connected to bus 11, but an SVC is connected at the PCC as shown in Fig. 5.10. The SVC is rated at 335 MVAr, where the rating is chosen intentionally to be over-sized in order to ensure that the amount of reactive power required to meet GIR discussed in the previous chapter is achievable. In addition, a fixed capacitor bank of 285 MVAr is connected to bus 3. The fixed capacitor bank is not included as part of the solar farm reactive power compensation since it is included simply to bring the voltage at the PCC above 0.95 pu without the solar farm connected. In practice, the sizing of fixed compensation and the SVC would be carefully considered in order to minimize the cost of the combined installation. However, for the purposes of this thesis, the results are simply intended to demonstrate the behavior of the solar farm power factor PF_{SF} and the PCC voltage V_3 assuming the necessary reactive power compensation is available.

The plot of Fig. 5.11(a) shows the power factor PF_{SF} of the solar farm over a range of SVC voltage set-points and irradiance. The results are obtained by setting the

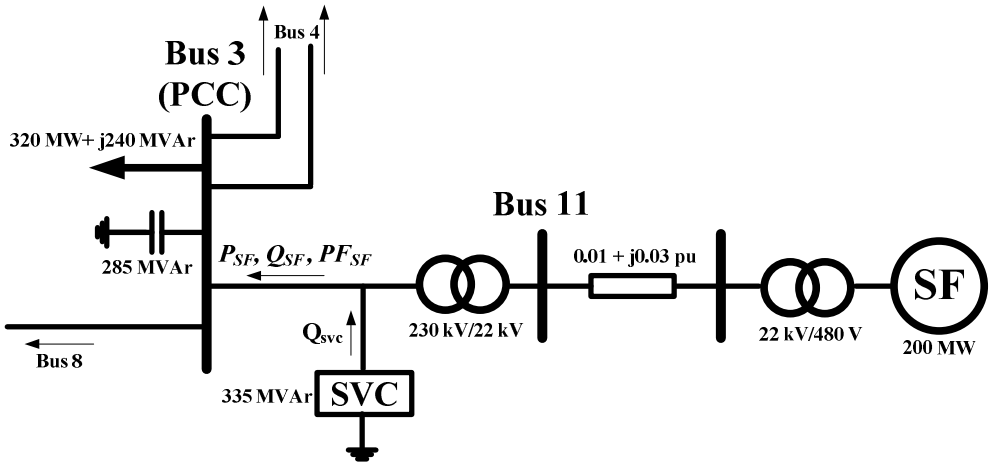

Figure 5.10: Connection of solar farm to bus 11 with an SVC used as variable reactive power compensation.

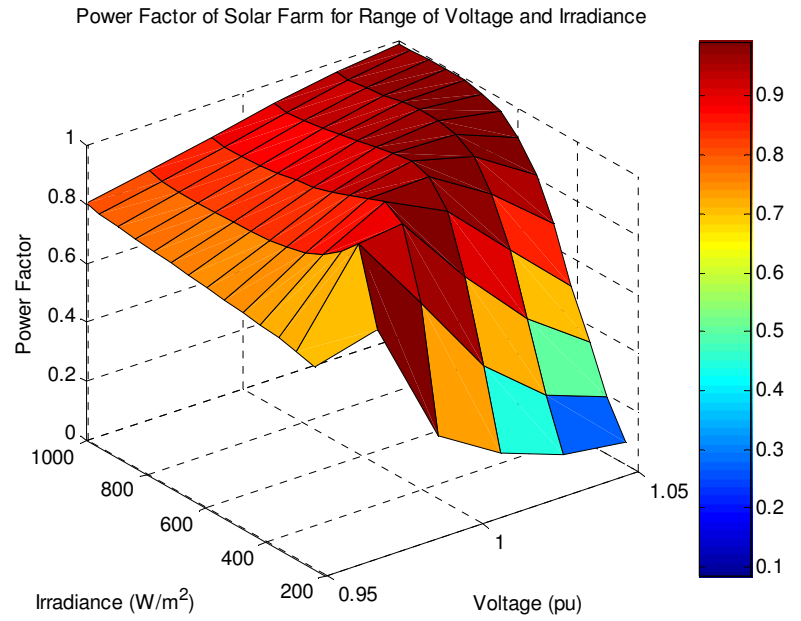

(a)

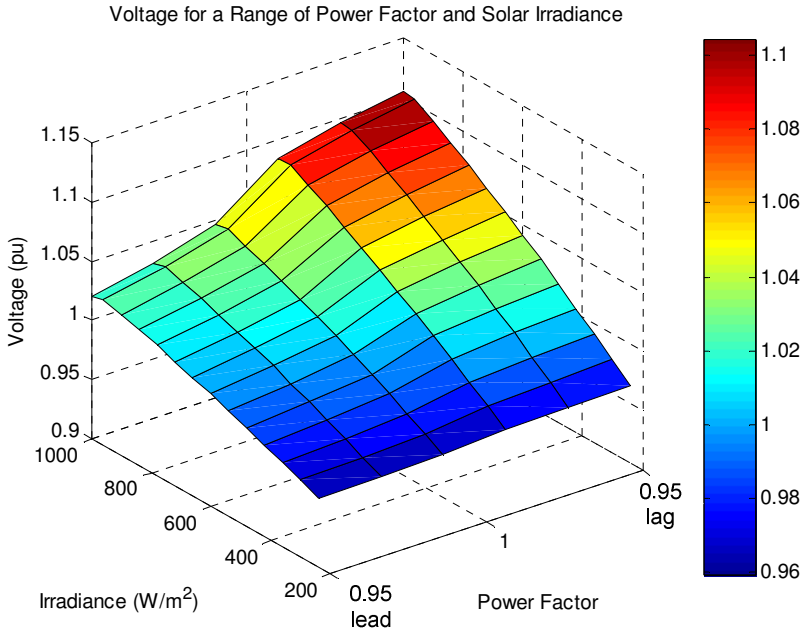

(b)

Figure 5.11: (a) Power factor PF_{SF} of the solar farm over a range of irradiance and voltage, with the SVC set to control voltage and (b) voltage at the PCC (bus 3) over a range of PF_{SF} and irradiance, with the SVC set to control PF_{SF}.

SVC to control the PCC voltage V_3 to a given level over the specified range of irradiance, supplying whatever quantity of reactive power is needed to maintain the commanded voltage level, which is defined in discrete steps over the range shown in Fig. 5.11(a). The results in Fig. 5.11(a) show that if the SVC is set to control voltage V_3, the power factor PF_{SF} moves outside the acceptable 0.95 lagging to 0.95 leading range for much of the irradiance and voltage range. The power factor becomes particularly poor as the irradiance decreases and the SVC voltage set point is at 1.05 pu. The power factor surface shown in Fig. 5.11(a) includes both leading and lagging power factors, but does not indicate the power factor orientation (leading or lagging) at a given voltage and irradiance point on the plot. The plot is designed to illustrate the effects of varying irradiance and voltage set points on the power factor *magnitude*, since the GIR specify that the power factor magnitude must be greater than 0.95, regardless of orientation.

The plot of Fig. 5.11(b) shows the voltage at the PCC with the SVC shown in Fig. 5.10 set to control the solar farm power factor PF_{SF}. The voltage V_3 remains within the acceptable region over most of the irradiance and PF_{SF} levels, accept for high irradiance and PF_{SF} values close to 0.95 lagging. The solar farm absorbs the maximum amount of reactive power at high irradiance, as shown in Fig. 4.5. Therefore, the SVC is required to supply the reactive power absorbed by the solar farm plus the additional amount required to bring its power factor PF_{SF} to 0.95 lagging. The excess reactive power causes the voltage to rise above 1.1 pu.

5.3.2.4 Variable Compensation with G3 AVR

The final case study for interconnection of a solar farm into the 12-bus network is shown in Fig. 5.12. In this case a 120 MW solar farm is connected to bus 3 of the network *in addition* to the base case 200 MW G3 plant at bus 11. The solar farm power rating is selected so that with an irradiance of 1000 W/m^2, the combination of G3 and the solar farm can meet the real power requirements of the 320 MW local load at bus 3. In

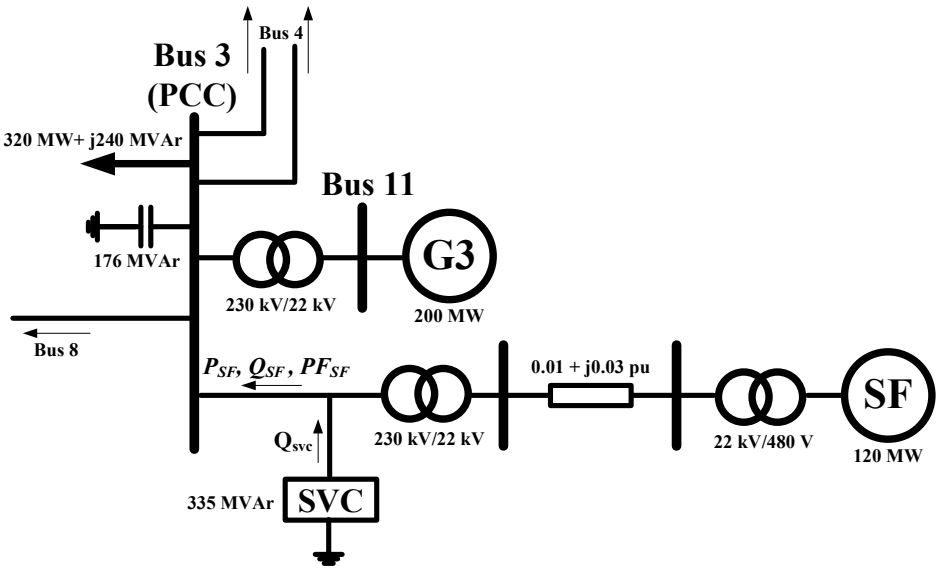

Figure 5.12: Interconnection of solar farm to bus 3 in addition to G3, with G3's AVR controlling the bus 11 voltage and the SVC controlling the solar farm power factor.

this case, the G3 AVR is used to control the voltage at bus 11, while the 335 MVAr SVC controls the power factor of the solar farm PF_{SF}. In addition, a 176 MVAr fixed capacitor bank is included at bus 3 to bring the power factor of G3 to unity in the absence of the solar farm, such as the case when the system would be operating during the night, when no irradiance were available.

A problem that can arise in using the G3 AVR to control the voltage at bus 11 is that it also must compensate for voltage drops at bus 3, since the impedance of the transformer between bus 3 and bus 11 is small. Therefore, G3's AVR effectively has to control the voltage of both its own terminals and that of bus 3. In this case, the power factor of G3 could potentially move out of an acceptable range in order to maintain the voltage set point at bus 11 since the solar farm's absorption of reactive power tends to reduce the voltage at bus 3 (and also bus 11). Simulation results of the power factor of G3 (bus 11) for varying solar farm power factor PF_{SF} and solar irradiance are shown in Fig. 5.13. The results indicate that G3's power factor stays relatively close to unity over the entire range of solar farm power factors and input solar irradiance, while maintaining

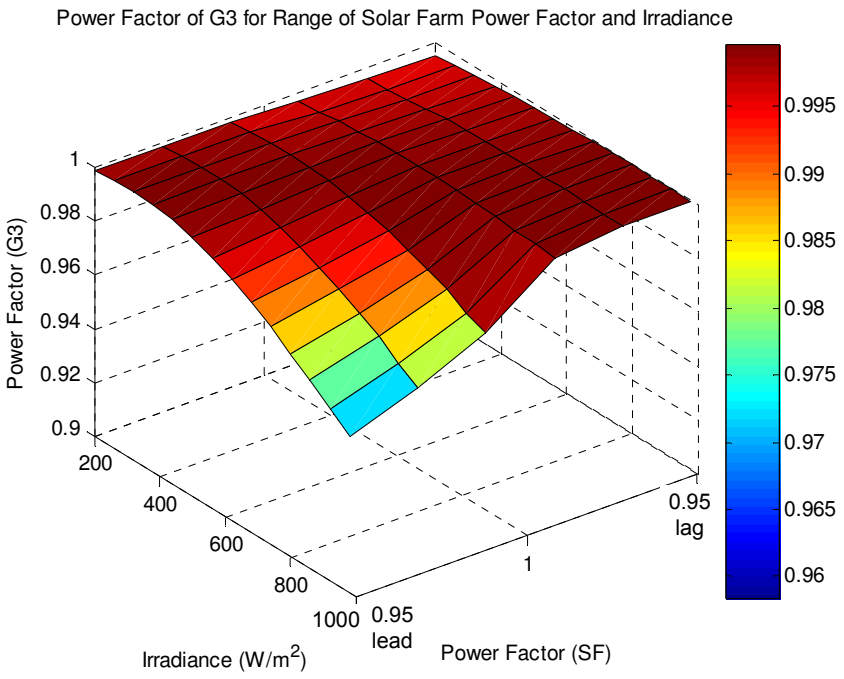

Figure 5.13: Power factor of G3 for a range of irradiance and solar farm power factor

the voltage at bus 11 at approximately 1 pu over the entire range. Thus the connection of the solar farm as shown in Fig. 5.12 to the 12-bus network is the only method in which both the power factor and voltage can be controlled within their acceptable limits over varying irradiance levels.

5.4 12- Bus Network Transient Analysis

5.4.1 Effects of Irradiance Level Variations

Simulation results for the SVC reactive power, real and reactive power of the solar farm, bus 3 voltage, induction generator speed, and G3 power factor are shown in Fig. 5.14(b-f) for the irradiance level variations of Fig. 5.14(a), where it is assumed that the irradiance level is the average over all of the individual DS units in the solar farm area. The solar farm is connected as shown in Fig. 5.12, and the SVC is set to control the power factor PF_{SF} of the solar farm to unity. As expected, the real power delivered by

the solar farm follows the irradiance level, as shown in Fig. 5.14(c). The reactive power of the solar farm is approximately zero during the cloud transient since the SVC is controlling the power factor PF_{SF} to be unity. Thus, all the reactive power generated by the SVC during the cloud transient, as shown in Fig. 5.13(b), is supplying the induction generator's reactive power needs. The voltage at bus 3, appearing in Fig. 5.14(d), deviates only slightly from 1 pu, indicating that the G3 AVR is capable of controlling the bus 3 voltage with the solar farm also connected to bus 3. The induction generator speed in Fig. 5.14(e) also varies with the irradiance level, but stays within a narrow operating range slightly above synchronous (1 pu) speed. Fig. 5.14(f) displays the power factor of G3, and shows that the power factor stays close to unity, indicating that the solar farm does not add any excessive reactive power burden to G3 even during varying irradiance levels.

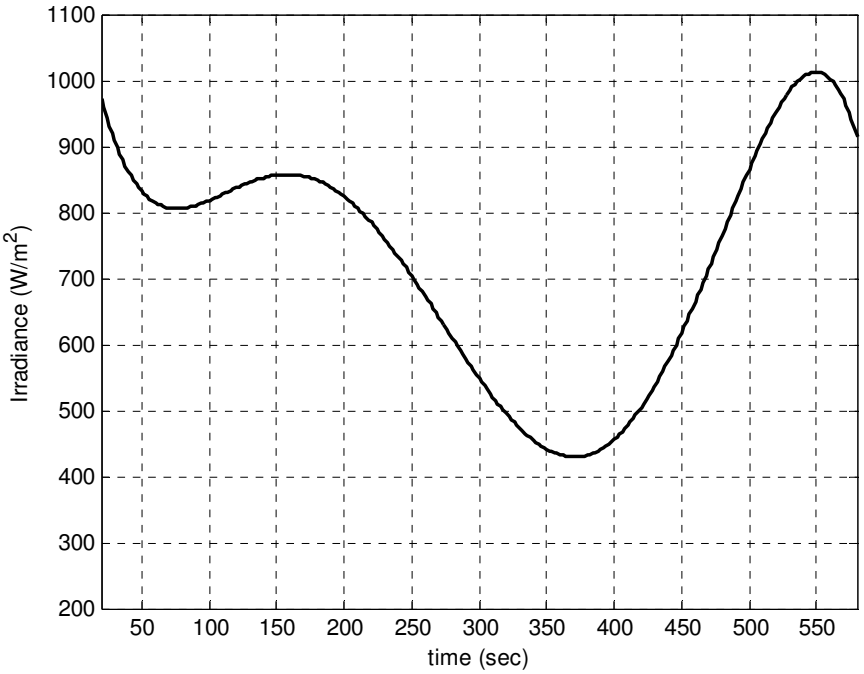

(a)

Figure 5.14: Simulation results of the solar farm (b) SVC reactive power output, (c) real and reactive power, (d) PCC (bus 3) voltage, (e) induction generator speed, and (f) G3 power factor for a cloud transient using the input irradiance waveform of (a).

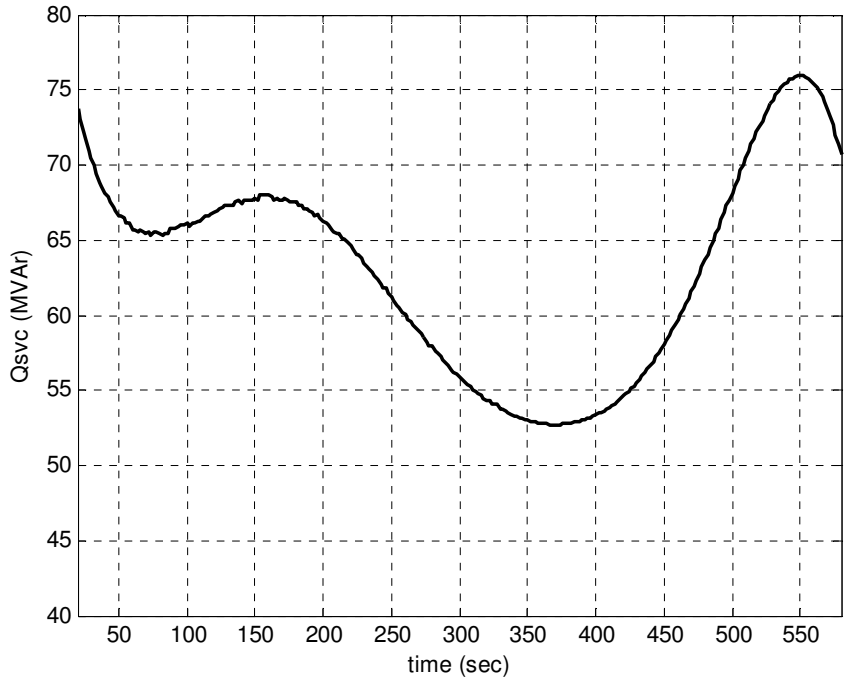

(b)

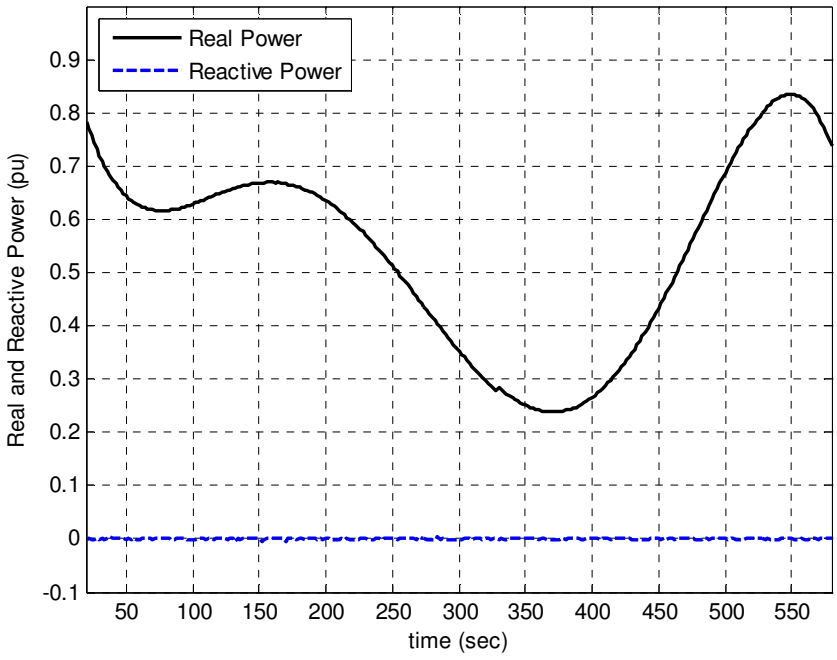

(c)

Figure 5.14 (cont'd): Simulation results of the solar farm (b) SVC reactive power output, (c) real and reactive power, (d) PCC (bus 3) voltage, (e) induction generator speed, and (f) G3 power factor for a cloud transient using the input irradiance waveform of (a).

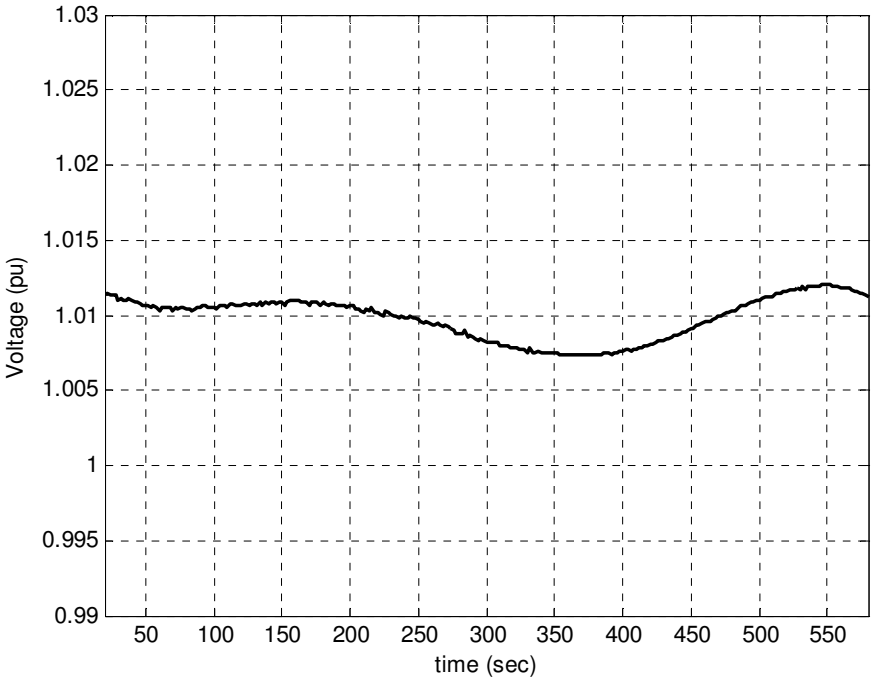

(d)

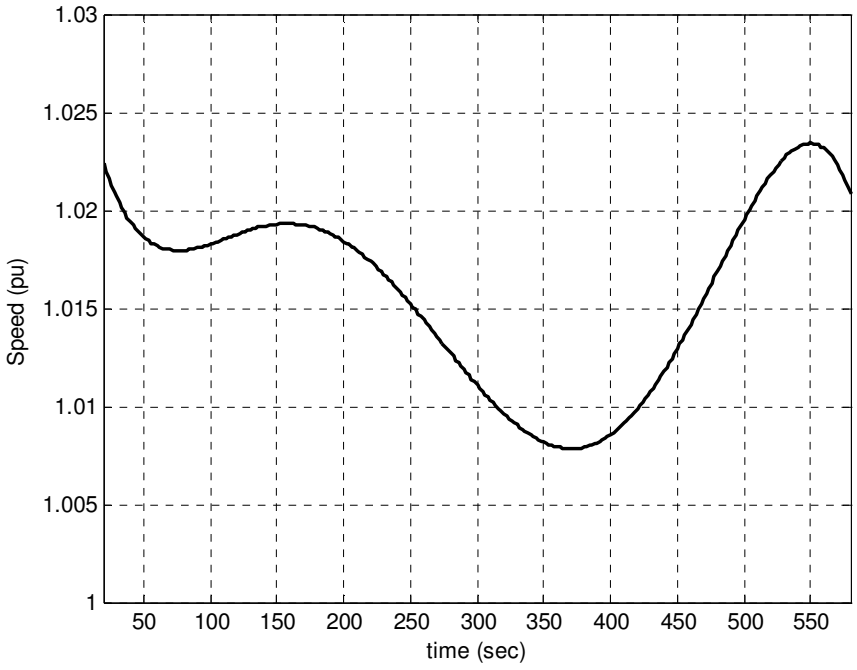

(e)

Figure 5.14 (cont'd): Simulation results of the solar farm (b) SVC reactive power output, (c) real and reactive power, (d) PCC (bus 3) voltage, (e) induction generator speed, and (f) G3 power factor for a cloud transient using the input irradiance waveform of (a).

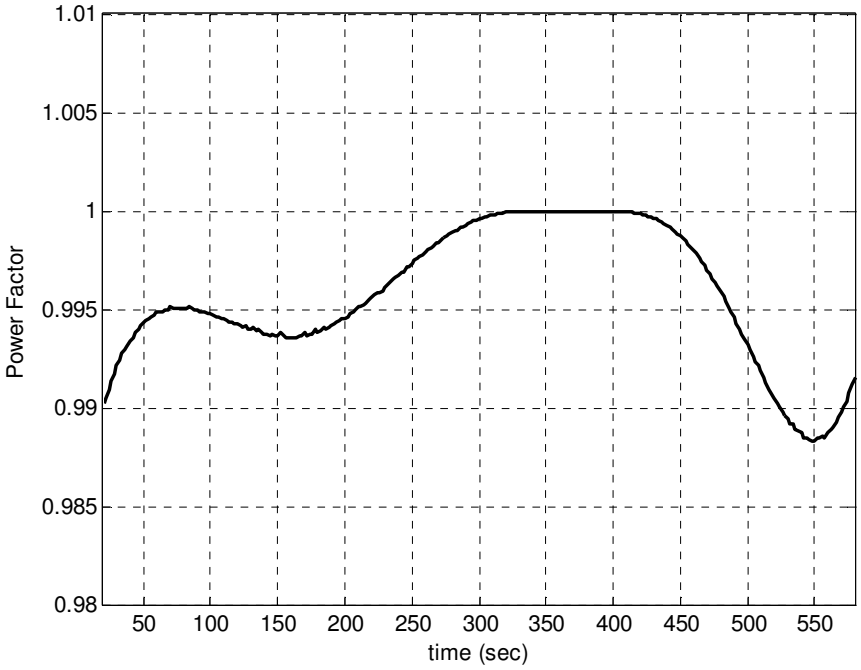

(f)

Figure 5.14 (cont'd): Simulation results of the solar farm (b) SVC reactive power output, (c) real and reactive power, (d) PCC (bus 3) voltage, (e) induction generator speed, and (f) G3 power factor for a cloud transient using the input irradiance waveform of (a).

5.4.2 Effects of a Three Phase Short Circuit

Simulation results for a 150 msec three phase short circuit applied to bus 3 are shown in Fig. 5.15. The solar farm is connected to the 12-bus network as shown in Fig. 5.12, with a constant irradiance level at 1000 W/m^2 applied to the solar farm. The fault resistance is zero, thus the voltage at bus 3 falls to zero during the fault, as shown in Fig. 5.15(a). The voltage recovers quickly after the fault is cleared due to G3's AVR and the SVC's injection of reactive power. The reactive power injected by the SVC is shown in Fig. 5.15(b), illustrating that the injected reactive power drops to zero during the fault since the voltage is zero. After the fault, the reactive power increases rapidly, causing the voltage to overshoot its pre-fault steady-state value. The real and reactive power output of the solar farm are shown in Fig. 5.15(c), and agree closely with the real and reactive

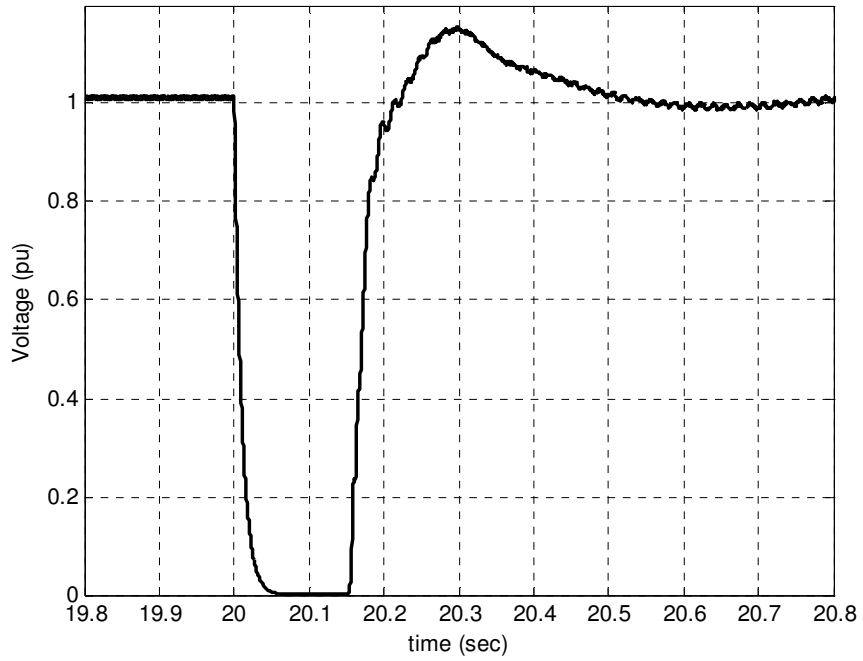

(a)

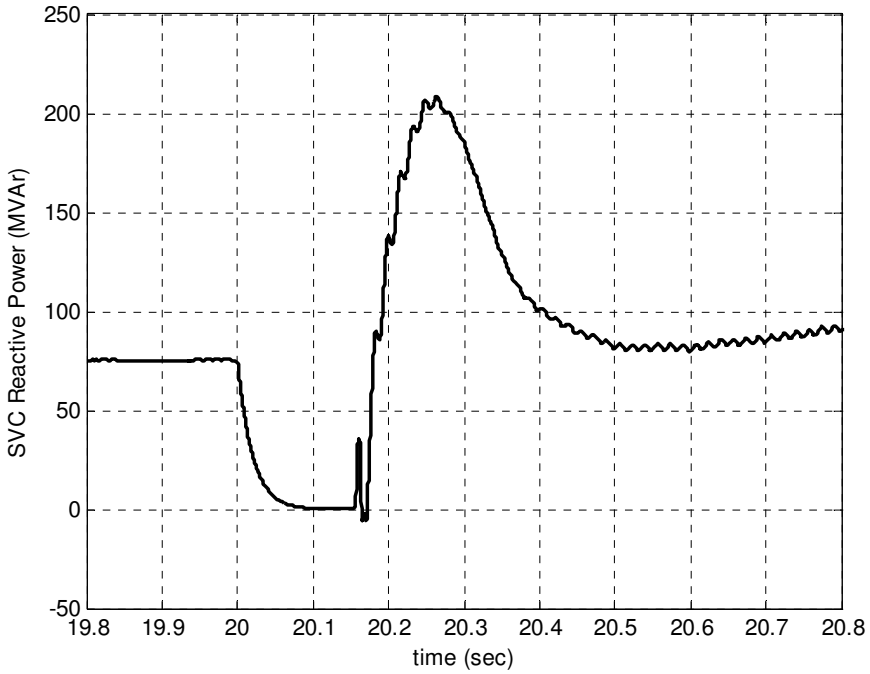

(b)

Figure 5.15: (a) Bus 3 voltage, (b) SVC reactive power, and (c) solar farm real and reactive power for a 150 msec three phase short circuit applied to bus 3.

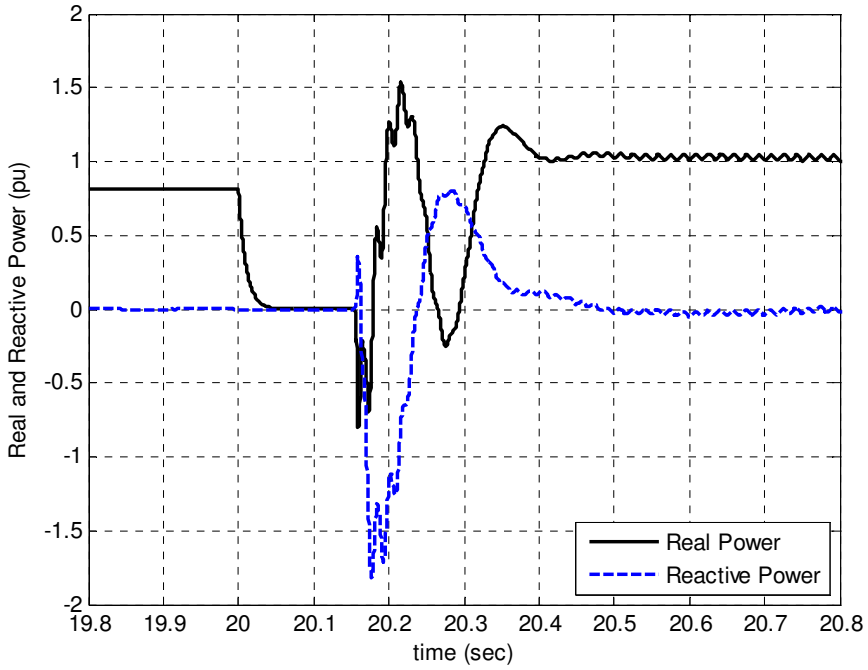

(c)

Figure 5.15 (cont'd): (a) Bus 3 voltage, (b) SVC reactive power, and (c) solar farm real and reactive power for a 150 msec three phase short circuit applied to bus 3.

power results for a three phase fault as applied to the SMIB model discussed in the previous chapter (see Fig. 4.8(e)). However, in the present results, an SVC is included with the solar farm, thus the reactive power actually increases above 0 during the post-fault recovery period, which indicates the solar farm is supplying reactive power to the network to help recover the voltage.

5.5 Conclusion

With no synchronous generator connected to bus 11, bus 3 can be considered a "weak" grid PCC. Therefore, adding a solar farm to a weak grid can be problematic, and for this study the steady state results show that the power factor and voltage requirements cannot both be met over all irradiance levels in the case of a 200 MW solar farm incorporated at bus 11. However, because the voltage can be brought to 1 pu with fixed capacitors at bus 3 with no power source connected to bus 11 (or bus 3), the solar farm

could be reduced in MW rating, which would decrease its impact on the voltage at bus 3 over varying irradiance levels and solar farm power factor. Therefore, in addition to varying irradiance levels due to cloud cover and the variable power factor requirement, the rating of the solar farm also plays an important part in determining whether the solar farm can meet the GIR.

When the solar farm is integrated into the 12-bus network near a synchronous generator, the PCC closely resembles a "strong" grid. In this scenario, the results with both G3 and the solar farm demonstrate that the solar farm can operate well within the power factor requirements, while G3 can maintain a suitable power factor. Therefore, the MW rating of the solar farm could potentially be increased, and the system would still be capable of meeting the GIR. Connecting the solar farm in this scenario also demonstrates good low voltage-ride through capability, where the SVC and G3 AVR can help recover the voltage quickly after the fault clears.

Simulation results for the various scenarios discussed above for integrating a solar farm into the 12-bus network illustrate the need for significant reactive power compensation in order to meet both voltage and power factor GIR. While the variable reactive power compensation discussed in this chapter has been over-sized to ensure that the solar farm could meet the GIR over all irradiance levels, in practice the variable reactive power compensation rating would have to be minimized in order to reduce cost. In addition, the effects of time-varying loads and grid connection requirements involving low voltage ride-through significantly affect the sizing of the reactive power compensation.

CHAPTER 6

CONCLUDING REMARKS

6.1 Conclusions

Dish-Stirling (DS) technology has the potential to meet a portion of future electricity needs with minimal environmental impact. Grid interconnection of the technology in large scale is both technologically feasible and potentially cost competitive with conventional power generation. However, because of the unique operating characteristics of DS systems, detailed system impact studies must be carried out to assess the effects of adding a large solar farm into a power network so as to not adversely affect system reliability. The work presented in this thesis provides a means for performing such detailed studies.

While the Stirling engine is a complex thermodynamic device, and has been treated as such in the literature, the purpose of this research is to model the *mechanical* characteristics (torque and speed) of the Stirling engine, rather than the thermodynamics. However, because the thermodynamic behavior of the engine ultimately affects the torque and speed characteristics, modeling of the thermodynamics is necessary. The research described in this thesis on the modeling of the DS system is not intended to be an exhaustive, detailed thermodynamic analysis of the DS system; rather, a detailed enough thermodynamic model is presented in order to accurately model the mechanical characteristics. Indeed, a much more detailed and thorough thermodynamic analysis is available in previous publications by others. An important study aspect of this study is to determine just how detailed the thermodynamic and working gas dynamic models have to be in order to achieve a reasonably accurate mechanical model for the purpose of power system simulation studies.

DS systems have demonstrated the highest efficiency of the CSP technologies, and potentially have a financial advantage over other technologies because more power can be produced from a DS system on a given day and location (assuming the same amount of land) than other technologies. However, DS systems currently have a higher initial capital costs than the other, more mature CSP technologies. In addition, other CSP technologies often use thermal energy storage, which can increase their capacity factors and smooth power variations under changing irradiance levels. Other CSP technologies use conventional synchronous generators, thus requiring no external reactive power compensation to meet GIR. Therefore, achieving low-cost systems is crucial for DS systems to remain competitive in the CSP and renewable energy markets.

6.2 Contributions

The work presented in this thesis provides a detailed analysis of a DS solar farm and its application in utility connected electric power generation. The models developed provide a means of analyzing the DS system's behavior under transient and steady state conditions for grid interconnection studies. Detailed models of the DS components, including the concentrator, receiver, Stirling engine, and induction generator, have been scattered throughout publications prior to the completion of this work, and provided little information regarding the behavior of a complete system, including the interaction between the various components during operation. The Stirling engine model developed in this thesis extends previous ideal adiabatic models of the engine to include the effects of varying heater temperature, varying working gas mass, and varying shaft speed. The control systems of a DS system have only been described in physical terms in previous work by others, and this thesis extends the general physical descriptions to detailed block diagrams and mathematical representations of the control systems, which enables a more thorough control system analysis and a basis for controller design. In addition, this thesis evaluates the grid interconnection issues associated with DS technology through

simulation studies, a topic which has yet to be investigated in publications to date. The grid interconnection case studies of Chapter 5 showed that extensive studies are required to assess reactive power compensation needs at interconnection points of DS solar farms, and topics such as solar farm size, grid "stiffness", local loads, local irradiance levels, and type of reactive power compensation must all factor in the planning studies.

Portions of the research presented in this thesis have been accepted for publication, and are given in [28], [29], and [30].

6.3 Recommendations

Recommendations for future work include experimental validation of the component models developed in this thesis. Various assumptions were made in the development of the DS model, and verification of the efficacy of such assumptions is required to ensure accurate dynamic models. The Stirling engine and receiver models in particular require extensive experimental validation due to the inherent complexity of these components. As for the receiver, the temperature of the absorber surface was assumed to be uniform over its entire surface, but variations in the temperature between the engine quadrants can significantly affect the dynamic characteristics of the DS system. In addition, losses within the receiver/absorber were assumed to be proportional to the difference in absorber temperature and ambient temperature, but more detailed studies of convective, conductive, radiation losses must prove whether this assumption is valid. In the Stirling engine model, the key assumptions of uniform pressure throughout the individual quadrants and adiabatic expansion and compression of the working gas should be validated. In addition, the thermal losses of the Stirling engine were neglected except for the regenerator model, which could prove to be inaccurate when compared to actual DS system operation. However, DS models developed for grid interconnection studies should focus on the impact of various parameters on the torque and speed characteristics of the Stirling engine, rather than aiming to provide detailed models of the

working gas or thermal characteristics of the engine. For power system studies, the primary concerns are the generator electrical characteristics and the prime mover torque and speed characteristics. Therefore, the thermal and gas dynamics are required only to model their impact on these key system parameters in steady state and transient conditions.

Further simulation studies are needed to assess a DS solar farm's behavior within a larger, more realistic network, which may include variable, non-linear loads. Optimization techniques for sizing the reactive power compensation are also needed, since the MVAr capacity of the compensation required will vary considerably among locations. Such optimization techniques can minimize the amount of reactive power compensation required, which can reduce installation costs. Other forms of generator technology should also be investigated, such as doubly fed induction generators and permanent magnet generators. While these technologies have a higher initial cost, the additional capital can be justified if more advanced generators can either reduce or eliminate the need for external reactive power compensation, which also requires significant investment.

APPENDIX A

DISH-STIRLING SYSTEM SIMULATION DATA

The gains used in the concentrator and receiver models, along with the Stirling engine dimensions discussed in Chapter 2 are provided in Table A.1 with the specified units. The working gas properties of the Stirling engine are listed in Table A.2. The specifications of induction generator and step-up transformers used in the simulations are provided in Tables A.3 and A.4, respectively. The various parameters for the control systems discussed in Chapter 3 are given in Table A.5.

Table A.1: Concentrator, Receiver, and Stirling Engine Simulation Data

Concentrator			
Concentrator Gain	K_C	79.85	m^2
Receiver			
Receiver Gain	K_R	0.005	K/J
Receiver Loss Gain	K_L	17	W/K
Stirling Engine			
Dead Space Volume (Expansion Space)	V_{de}	1.0000E-05	m^3
Dead Space Volume (Compression Space)	V_{dc}	1.0000E-05	
Piston Swept Volume	V_s	9.5000E-05	
Cooler Volume	V_k	2.5447E-04	
Regenerator Volume	V_r	2.2455E-04	
Heater Volume	V_h	3.3080E-05	
Cooler Temperature	T_k	323.16	K
Displacement Angle (Expansion Space)	α_e	0	degrees
Displacement Angle (Compression Space)	α_c	90	degrees

Table A.2: Working Gas Properties

Working Gas: Hydrogen			
Gas Constant	R	4120	m^3*Pa/(K*kg)
Specific Heat Capacity (Constant Pressure)	c_p	14570	J/(K*kg)
Specific Heat Capacity (Constant Volume)	c_v	10450	J/(K*kg)
Ratio of Specific Heats	γ	1.39	-

Table A.3: Induction Generator Specifications

Induction Generator			
Rated Voltage	V	460	Volts (rms)
Rated Current	I	35.14	A
Rated Frequency	f	60	Hz
Rated Power Factor	pf	0.87	-
Rated Efficiency	η	0.938	-
Rated Slip	$slip$	0.0133	pu
Starting Current	I_{st}	6.2	pu
Starting Torque	τ_{st}	1.57	pu
Max Torque	τ_{max}	2.88	pu
Moment of Inertia	J	0.535	s
Mechanical Damping	F	0.01	pu
poles	$poles$	4	-

Table A.4: Step-Up Transformer Specifications

Step-Up Transformer		
VA Rating	28000	VA
Primary Winding	480	Volts
Secondary Winding	22000	Volts
Pos. Seq. Leakage Reactance	0.05	pu
Magnetizing Current	1	%
No-Load Losses	0	pu
Copper Losses	0	pu

Table A.5: Control System Parameter Values

Control System Parameters			
Solenoid Valve Gain	K_v	1	-
Solenoid Valve Time Constant	T_v	0.02	s
Solenoid Valve Maximum Flow	MF_{max}	0.08	kg/s
Heater Temperature Set Point	T_{set}	993	K
Heater Temperature Control Region	ΔT_{max}	50	K
Over-Speed Threshold	ω_{set}	1.05	pu
Minimum Command Pressure	p_{min}	2	MPa
Maximum Command Pressure	p_{max}	25	MPa

REFERENCES

[1] U.S. Energy Information Administration, Report No. DOE/EIA-0383: Annual Energy Outlook 2010 with Projections to 2035 [Online], April 2010. Available: www.eia.doe.gov/oiaf/aeo/

[2] National Renewable Energy Laboratory. (2010, Mar.). *Concentrating Solar Power Projects* [Online]. Available: http://www.nrel.gov/csp/solarpaces/

[3] Images Source: http://wikipedia.org/

[4] National Renewable Energy Laboratory, Report No. NREL/TP-620-39726: Power Technologies Energy Data Book, Fourth Edition [Online], August 2006. Available: http://www.nrel.gov/analysis/power_databook/docs/pdf/39728_complete.pdf

[5] U.S. Department of Energy, Solar Energy Technologies Program: Multi Year Program Plan 2008-2012 [Online], April 2008. Available: http://www1.eere.energy.gov/solar/pdfs/solar_program_mypp_2008-2012.pdf

[6] Stirling Energy Systems. (2010, Jun.). *SES-Tessera Solar Corporate Video* [Online]. Available: http://www.stirlingenergy.com/

[7] Stirling Energy Systems. (2008, Feb.). *Sandia, Stirling Energy Systems Set New World Record for Solar-to-Grid Conversion Efficiency* [Online]. Available: http://www.stirlingenergy.com/pdf/2008-02-12.pdf

[8] T. Mancini, P. Heller, B. Butler, et. al, "Dish-Stirling Systems: An Overview of Development and Status," in *Journal of Solar Energy Engineering*, vol. 125, pp. 135-151, May 2003.

[9] Tessera Solar. (2010, Jan.). *Tessera Solar and Stirling Energy Systems Unveil World's First Commercial Scale Suncatcher™ Plant, Maricopa Solar, with Utility Partner Salt River Project* [Online]. Available: http://tesserasolar.com/north-america/pdf/2010_01_22.pdf

[10] W. B. Stine and R. B. Diver, "A Compendium of Solar Dish/Stirling Technology." Sandia National Laboratories, Report SAND93-7026 UC-236, January 1994.

[11] G. Walker, *Stirling Engines*. Oxford: Clarendon Press, 1980. (ISBN # 0198562098)

[12] C. W. Lopez and K. W. Stone, "Performance of the Southern California Edison Company Stirling Dish" Sandia National Laboratories, DOE Contract DE-AC04-94AL85000, October 1993.

[13] G.T. Reader and C. Hooper, *Stirling Engines.* London: E. & F.N. Spon, 1983. (ISBN # 0419124004)

[14] T. Finkelstein, "Thermodynamic Analysis of Stirling Engines." in *J. Spacecraft*. 1967.

[15] T. Finkelstein, "Analysis of Practical Reversible Thermodynamic Cycles," in *AIChE-ASME Heat Transfer Conference and Products Show*, August 9-12, 1964, Cleveland, Ohio.

[16] T. Finkelstein, "Computer Analysis of Stirling Engines," in *Proc. 10th Intersociety Energy Conversion Engineering Conference*, pp. 933-941, 1975.

[17] I. Urieli, "The Ideal Adiabatic Cycle-A Rational Basis for Stirling Engine Analysis," in *Proc. 17th Intersociety Energy Conversion Engineering Conference*, vol. 4, pp. 1662-1668, 1982.

[18] D.G. Thombare and S.K. Verma, "Technological Development in the Stirling Cycle Engines," in *Renewable and Sustainable Energy Reviews*, vol. 12, issue 8, pp. 1-38, Jan. 2008.

[19] K.O. Lund, "A Direct-Heating Energy-Storage Receiver for Dish-Stirling Solar Energy Systems," ASME, *Journal of Solar Energy Engineering*, vol. 118, pp. 15-19, February 1996.

[20] R.E. Hogan, Jr., "Numerical Modeling of Reflux Solar Receivers," in *Journal of Solar Energy Engineering,* vol. 115, pp. 93-100, May 1993.

[21] R.E. Hogan, R.B. Diver, and W.B. Stine, "Comparison of Cavity Solar Receiver Numerical Model and Experimental Data," in *Journal of Solar Energy Engineering*, vol. 112, pp. 183-190, August 1990.

[22] F. Nepveu, A. Ferriere, and F. Bataille, "Thermal Model of a Dish/Stirling Systems" in *Solar Energy*, vol. 83, pp. 81-89, Jan. 2009.

[23] J.J. Droher and S.E. Squier, "Performance of the Vanguard Solar Dish-Stirling Engine Module," Electric Power Research Institute, Report EPRI AP-4608, July 1986.

[24] B. J. Washom, "Vanguard 1 Solar Parabolic Dish-Stirling Engine Module," Advanco Corporation, DOE Contract DE-FC04-82AL16333, Sep.1984.

[25] Y. Zhang and B. Osborn, "Solar Dish-Stirling Power Plants and Related Grid Interconnection Issues," in *Proc. 2007 IEEE PES General Meeting*, Jun. 24-28, 2007, Tampa, FL.

[26] S.H. Almstrom, C. Bratt, and H.G. Nelving, "Control Systems for United Stirling 4-95 Engine In Solar Application," in *Proc.16th Intersociety Energy Conversion Engineering Conference*, Aug. 9-14, 1981, Atlanta, GA.

[27] H. Lemrani and P. Stouffs, "Dynamic Simulation of Kinematic Stirling Engines Applied to Power Control," in *Proc. 29th Intersociety Energy Conversion Engineering Conference*, vol. 4, pp. 1896-1901, 1994.

[28] D. Howard and R.G. Harley, "Modeling of Dish-Stirling Solar Thermal Power Generation," in *Proc. 2010 IEEE Power Engineering Society General Meeting*, Jul. 25-29, 2010, Minn., MN. [Accepted].

[29] D.F. Howard, J. Liang, and R.G. Harley, "Control of Shaft Speed and Receiver Temperature in Dish-Stirling Solar Power Generation for Power Grid Integration," in *Proc. 2010 IEEE Energy Conversion Congress & Exposition*, Sept. 12-16, 2010, Atlanta, GA. [Accepted].

[30] D.F. Howard, R.G. Harley, J. Liang, and G.K. Venayagamoorthy, "Effects of Variable Solar Irradiance on the Reactive Power Compensation for Large Solar Farm," in *Proc. 2010 IEEE International Institute for Research and Education in Power Systems Symposium*, Aug. 1-6, 2010, Rio de Janeiro, Brazil. [Accepted].

[31] I. Urieli. (2010, Jan. 1). *Stirling Cycle Machine Analysis* [Online]. Available: http://www.ent.ohiou.edu/~urieli/stirling/me422.html.

[32] M. Taghizadeh, A. Ghaffari, and F. Najafi, "Modeling and Identification of Solenoid Valve for PWM Control Applications," in *Comptes Rendus Mecanique*, vol. 337, no. 3, pp. 131-140, Mar 2009.

[33] Federal Energy Regulatory Commission, Regulatory Order No. 661: Interconnection for Wind Energy [Online], June 2, 2005. Available: http://www.ferc.gov/industries/electric/indus-act/gi/wind.asp.

[34] Federal Energy Regulatory Commission, Regulatory Order No. 661-A: Interconnection for Wind Energy [Online], December 12, 2005. Available: http://www.ferc.gov/industries/electric/indus-act/gi/wind.asp.

[35] S. Jiang, U.D. Annakkage, and A.M. Gole, "A Platform for Validation of FACTS Models," in *IEEE Transactions on Power Delivery*, Vol. 21, No. 1, Jan. 2006.

[36] National Renewable Energy Laboratory. (2010, Jun.). *Renewable Resource Data Center* [Online]. Available: http://www.nrel.gov/rredc/solar_resource.html